Binary mixtures in two dimensions

Inaugural-Dissertation
zur Erlangung des Doktorgrades
der Mathematisch-Naturwissenschaftlichen Fakultät
der Heinrich-Heine-Universität Düsseldorf

vorgelegt von
Lahcen Assoud
aus Düsseldorf

April 2010

Aus dem Institut für Theoretische Physik II: Weiche Materie
der Heinrich-Heine-Universität Düsseldorf.

Gedruckt mit der Genehmigung
der Mathematisch-Naturwissenschaftlichen Fakultät
der Heinrich-Heine-Universität Düsseldorf

Referent: Prof. Dr. Hartmut Löwen
Koreferent: Priv. Doz. Dr. René Messina

Tag der mündlichen Prüfung:

The work described in this thesis has been published in a number of papers, which constitute the following self-contained chapters:

- **Chapter 1**: L. Assoud, R. Messina, H. Löwen, "Binary crystals in two-dimensional two-component Yukawa mixtures," *J. Chem. Phys.* (2008), 164511
- **Chapter 2**: L. Assoud, R. Messina, H. Löwen, "Stable crystalline lattices in two-dimensional binary mixtures of dipolar particles," *Europhys. Lett. 80* (2007), 48001.
- **Chapter 3**: L. Assoud, F. Ebert, P. Keim, R. Messina, G. Maret, H. Löwen, "Crystal nuclei and structural correlations in two-dimensional colloidal mixtures: experiment versus simulation," *J. Phys.: Condens. Matter 21* (2009), 464114 .
- **Chapter 4**: L. Assoud, F. Ebert, P. Keim, R. Messina, G. Maret, H. Löwen, "Ultrafast Quenching of Binary Colloidal Suspensions in an External Magnetic Field," *Phys. Rev. Lett. 102* (2009), 238301.
- **Chapter 5**: L. Assoud, R. Messina, H. Löwen, "Ionic mixtures in two dimensions: from regular to empty crystals," *Europhys. Lett. 89*(2010), 36001.

The author was also involved in the following publications, which are not part of this thesis:

- H. Löwen, C. N. Likos, L. Assoud, R. Blaak, and S. van Teeffelen, "Critical nuclei and crystallization in colloidal suspensions," *Philos. Mag. Lett. 87* (2007), 847 .
- L. Assoud, R. Messina, "Penalty Method: application in soft matter," in preparation.
- H. Löwen, E. C. Oğuz, L. Assoud, R. Messina, "Colloidal crystallization between two and three dimensions," submitted to Advances in Chemical Physics.

Summary

In this thesis, we present recently obtained results on binary colloidal mixtures in two dimensions. It contains three parts, each deals with a different typical colloidal system, characterized by a class of pair interactions.

In the first part, we study the zero-temperature phase diagram of binary mixtures of like-charged particles interacting via a screened Coulomb pair potential. The ground-state (i.e. zero-temperature) phase diagram for a two-component Yukawa monolayer has been determined, via lattice sums calculations, at various pressures for arbitrary compositions and a broad range of charge asymmetries. A wealth of different composite lattices have been found to be stable and it is observed that the larger the charge asymmetry, the more complex the phase diagram becomes.

In the second, part we focus on the crystallization of binary mixtures of supermagnetic colloidal particles confined at a two dimensional water-air interface. Using lattice sums, the phase diagram is computed at zero temperature as a function of composition and the ratio of their magnetic susceptibilities. In addition, we employ Monte Carlo computer simulations to investigate this system. In the simulations, the interaction is modelled as a pairwise dipole-dipole repulsion. While the ratio of the magnetic dipole moments is fixed, the dipolar interaction strength governed by the external magnetic field and the relative composition is varied. Excellent agreement between simulation and experiment is found when comparing the partial pair distribution functions including the fine structure of the neighbour shells at high coupling. These mixtures exhibit local crystal nuclei in the melt, which can be identified by bond-orientational order parameters and their contribution to the pair structure is discussed. Furthermore, we realize a virtually instantaneous cooling, which is impossible in molecular systems, by a sudden increase of the external magnetic field. Using Brownian dynamics computer simulations, the relaxation behavior after such a quench is explored. Local crystallites with triangular and square symmetry are formed on different time scales and the correlation peak amplitude of the small particles evolves nonmonotonically in time in agreement with experiments.

The third part deals with two-dimensional ionic mixtures composed of oppositely charged spheres. The ground state at zero pressure is determined as a function of the size asymmetry by using a novel penalty method. We consider two different set-ups, the “interfacial model” and the “substrate model”. In the interfacial model which can be considered as a purely two-dimensional situation, the centres of all spheres are confined to a plane. In the substrate model, on the other hand, all spheres are touching the same underlying plane. The cascade of stable structures includes square, triangular and rhombic crystals as well as “empty” crystals made up of dipoles and chains, which have a vanishing number density. We confirm the square structure, found experimentally on charged granulates.

Zusammenfassung

Die vorliegende Arbeit besteht aus drei Hauptprojekten, in denen drei verschiedene kolloidale Suspensionen studiert werden.

Im ersten Teil untersuchen wir die Phasenverhalten von binären geladenen kolloidalen Mischungen in zwei Dimensionen im Grundzustand ($T = 0$), deren Wechselwirkung mit einem Yukawa-Paarpotential beschrieben wird. Mit Hilfe der Gittersumme wird die freie Enthalpie pro Teilchen minimiert. Die Maxwell-Konstruktion wird benutzt, um die globalen Phasendiagramme unseres Systems als Funktion der Komposition und des Ladungsverhältnisses zu berechnen.

Im zweiten Teil der Arbeit analysieren wir die Wechselwirkung von Mischungen aus superparamagnetischen Kolloiden unter dem Einfluss eines äußeren Magnetfeldes. Die Partikel sedimentieren an einer Wasser-Luft Grenzfläche eines Wassertropfens. Das System kann als ideal zweidimensionalen betrachten werden, da die vertikalen Bewegungen der Teilchen klein im Vergleich zum Teilchendurchmesser sind. Das zu dieser Ebene senkrecht stehende magnetische Feld induziert in den Partikeln magnetische Dipolmomente und führt zu einer repulsiven Teilchenwechselwirkung. Die stabilen Phasen im Grundzustand werden als Funktion von Dipolstärkenverhältnis und Komposition mit Hilfe der effizienten Leknersummation bestimmt. Für endliche Temperaturen werden mit Hilfe der Monte Carlo Simulationsmethode die radialen Paarkorrelationsfunktionen berechnet und mit denen von Experimenten verglichen. Außerdem werden lokale Kristallnukleationen durch Bond-Order Parameter identifiziert. Durch eine Änderung des externen Magnetfeldes kann die effektive Systemtemperatur leicht kontrolliert werden. Eine ultraschnelle Abkühlung (Quench) kann durch eine schnelle Erhöhung des externen Magnetfeldes auf einer Zeitskala von Milisekunden realisiert werden. Dies ist mit atomaren oder molekularen Systemen nicht zu erreichen. Die quadratischen und hexagonalen kristallinen Bereiche können direkt nach dem Quench bestimmt und ihr Wachstum zeitlich verfolgt werden. Die Daten aus dem Experiment von Ebert et al. zeigen sehr gute Übereinstimmungen mit den Ergebnissen unserer Brownsche Dynamik (BD)-Simulationen.

Im letzten Teil geht es schießlich um eine zweidimensionale ionische Mischung aus entgegengesetzt geladenen Kugeln. Wir beschäftigen uns hier mit dem Grundzustand des Systems bei verschwindendem Druck ($p = 0$). Mit Hilfe einer neuen Methode (Penalty), die Minimierungprobleme bei harten Kugeln aufhebt, wird eine Kaskade von stabilen Strukturen (quadratische, dreieckige, rhombische Kristalle und sogenannten “empty” Kristalle) gefunden. Die Quadratstruktur ist in granularen Systemen experimentell bestätigt worden.

Acknowledgments

I would like to express my thanks:

- to Hartmut Löwen who was always actively involved in my work. It was an honor to have him as my teacher and supervisor. His ideas and advices have contributed to the success of this work.
- to René Messina for his immense support and guidance. I was in the fortunate position to have them almost at any time available for discussions. It has been a pleasure to work with him and to learn more french idioms.
- to all members of the institute. Jo, thank you for your patience with all my technical problems. I owe very special thanks to Dr. Martin Rex, Dr. Sven van Teeffelen, Dr. Adam Wysocki, Dr. Ronald Blaak, Erdal C. Oğuz and Sebastian Huißmann for constructive discussions.
- to my wife for all her love and support that she had given to me.

Contents

Introduction

The thesis at hand deals with the study of two-dimensional colloidal crystals with long-ranged and short-ranged interactions. These systems belong to the field of physics known as *soft matter*, which is synonymous to "complex fluids" and "colloidal systems" [1]. Soft matter systems consist of particles with typical sizes between $1nm$ and $1\mu m$, so-called "mesoscopic" particles, and include liquids, colloids, polymers, foams, gels, granular materials, and a number of biological substances. Colloidal science (also called the study of colloidal suspensions) has been introduced in 1861 by the Scottish scientist Thomas Graham, who noticed that some substances like gelatine, caramel and starch diffuse more slowly than substances like salt, alcohol and sugar [2]. Colloidal particles are significantly larger than atoms but much smaller than macroscopic objects. Being mesoscopic, colloidal particles are small enough to exhibit collective behaviour similar to that of atomic systems. An example of this analogy is the similarity in structure and phase diagrams. However, due to their large size, colloidal particles have in many aspects a different collective behaviour in comparison to atoms and micro-molecules. For example, atomic system has a relaxation time of the order of 0.1 ps whereas this time is shifted to $1 - 10000$ ns for a colloidal suspension [3]. We may get a better understanding of molecular and colloidal systems by comparing corn schnapps and milk. Schnapps is a molecular liquid whereas milk is a colloidal one [1].

Crystallization is a central topic in condensed matter physics and is of great importance for many applications in material science chemistry, geographic and polymer physics [4]. Colloidal crystals are studied, for example, to understand phenomena such as freezing and melting [3]. The interparticle potentials in such colloidal crystals are in most cases precisely known and, more importantly, externally controllable. Moreover, the relevant time and length scales in colloidal systems are comparatively easy to access experimentally. Both aspects suggest that their study directly enables us to probe the connection between microscopic interaction potentials and macroscopic crystal properties. An other major topic is the study of glasses which are important in many industrial applications and are a part of daily life. A glassy state is formed if crystallization is avoided upon cooling or increasing density [5]. The interplay between vitrification and crystallization has been discussed in detail in for instance Ref. [6].

The macroscopic behaviour of crystalline systems sensitively depends on the dimensionality. Consider, for instance, the crystallization in two dimensions: a classical problem has been formulated since KTHNY theory of melting for 40 years. According to this theory, which has been developed by Kosterlitz-Thouless-Halperin-Nelson-Young, melting is based on the decoupling of pairs of topological defects and it predicts the existence of an intermediate equilibrium phase, namely the *hexatic* phase, between the crystal and the liquid state [7–9]. The prediction of this theory was successfully confirmed experimentally by Maret and co-workers using video microscopy and image processing [10–12].

The situation is much more complex for binary mixtures in two-dimensions because multicomponent mixtures show an enormously rich phase behaviour than one-component systems [13,14]. In particular, a fluid may freeze into many more diverse class crystal structures than is possible for one-component fluids.

Why should we be interested in binary mixtures? The first reason is that for mixtures of hard disks a wealth of close-packed [15] and thermodynamically stable [16] binary crystalline structures already exist. Our aim is to understand the topology of phase diagrams for systems of binary mixtures with various explicit forms of the interaction potentials. The second reason is technological. Most systems in nature and technology are mixtures of differently sized (charged) particles. Each distinct particle size (charge) introduces another length scale, which gives rise to an especially rich phenomenology in comparison with one-component systems.

In the present thesis we investigate Yukawa, dipolar pointlike particles and oppositely charged sphere mixtures. The Yukawa (screened Coulomb) potential is a widely used description for an effective pair interaction in charged colloidal suspensions [17] and dusty plasmas [18]. Highly charged colloidal suspensions confined between charged parallel glass plates [19–21], which restricts their motion practically to two dimensions, exhibit structural and dynamical behaviour quite different from the corresponding bulk state [22,23]. The interaction between these mesoscopic particles is described by an intermediate screened Coulomb Yukawa pair potential [24] which involves the screening length as an additional parameter in the system, resulting in even more possible complexity in the topology of the phase diagram. Such crystalline monolayers can also be realized experimentally for a confined binary mixture of like-charged colloids [19]. Another realization of two-dimensional Yukawa particles are dusty plasma sheets [25]. The two known extreme limits of zero and infinite screening length corresponding to hard disks [15] and the unscreened Coulomb case [26] are recovered. At various pressures for arbitrary compositions and a broad range of charge asymmetries, the ground-state (i.e. zero-temperature) phase diagrams have been explored. The predicted structures are observed in experiments on confined mixtures of like-charge colloids or dusty plasma sheets.

Two-component (binary) systems with large and small magnetic dipole moments represent ideal glass formers in two spatial dimensions [27–30]. In experiments, colloidal glasses have the advantage over atomic system that single particle resolution is provided by microscopy [27, 31–33]. The idea here is to consider two kinds of spherical and super-paramagnetic colloidal particles with different diameters and thereby magnetic susceptibilities, which are confined by gravity to an air-water interface formed by a pending water drop [34]. To this, a magnetic field $\mathbf{H}$ is applied perpendicularly to the water-air interface which induces magnetic dipole moments in the particles, of the form $\mathbf{m} = \chi \mathbf{H}$, χ being the magnetic susceptibility. This leads to a repulsive dipole-dipole pair interaction between the particles which can be described by a pairwise potential $\propto 1/r^3$ [35]. The zero-temperature phase diagram was calculated by lattice sums as a function of composition and the ratio of their magnetic susceptibilities (see Chapter 2), showing a variety of different stable solid lattices. The topology of the phase diagram is different from that of hard disks.

The theoretical prediction of crystal nucleation formation is still far from being explored and understood [36–38]. Binary mixtures of super-paramagnetic colloids confined to an air-water interface are excellent model systems for studying crystal nucleation [30], crystallization [13] and glass formation [39] in real space. By controlling an external magnetic field, the interparticle interactions can be tuned. In this thesis we study the local crystallites in the bulk. Furthermore, we find an excellent agreement between Monte Carlo computer simulation and experiment for the partial pair distribution functions (see Chapter 3). Since the magnetic field strength corresponds to temperature, an ultrafast temperature quench can be realized experimentally, which is very difficult for molecular systems. In Chapter 4, we show that an ultrafast quenching is possible for colloidal particles on the diffusive time scale of their motion. We perform nonequilibrium Brownian dynamics (BD) computer simulations and we compare them to experiments. Both, experiments and Brownian dynamics computer simulation data are in good agreement.

The third model system under study, described in Chapter 5, is a two-component mixture of oppositely charged particles in two spatial dimensions. Due to a hard core part in the potential, a new technique, the so-called *penalty* method, has been applied to overcome this difficulty. This method is developed to eliminate some or all of the constraints and add to the potential energy a penalty term which prescribes a high cost to infeasible points. By minimizing the Madelung potential energy per particle pair with respect to various periodic equimolar candidate lattices, the ground state of the system at zero temperature and zero pressure is explored. Our motivation for studying the ionic mixtures in two dimensions is twofold. First, and more fundamentally, the stability of two-dimensional ionic monolayers has not been addressed for differently sized ions. Previous theoretical studies focused on ionic criticality [40] at finite temperature and on equal ion size [41]. Second, two-dimensional ionic crystals can be experimentally realized on microscopic, mesoscopic and macroscopic length scales. Two set-ups are considered, the “interfacial model” in which all centers of mass belong to a common plane, and the “substrate model” in which all particle surfaces touch a common plane.

The outline of the thesis is organized as follows: in Chapter 1 the ground-state phase diagram for a two-component Yukawa monolayer at various pressures is studied for arbitrary compositions and a broad range of charge asymmetries. In Chapter 2, 3 and 4 we introduce the model of a two-component system of parallel dipoles.

This model can be realized in magnetic colloidal suspensions confined to an air-water interface. The zero-temperature phase diagram is explored in Chapter 2. In Chapter 3 we consider the model presented in the preceding Chapter 2. Results of experiments and Monte Carlo computer simulations are presented and discussed. Chapter 4 discusses the realization of an ultrafast quench in two-dimensional colloidal mixtures. The magnetic field can be almost instantaneously be changed on the diffusive time scale of motion of the colloidal particle. The experimental data are compared with Brownian dynamic computer simulation.

Finally, in Chapter 5, the stable ground state structures of two-dimensional ionic crystals at zero pressure are explored.

Chapter 1

Binary crystals in two-dimensional two-component Yukawa mixtures [1]

Abstract

The zero-temperature phase diagram of binary mixtures of like-charge particles interacting via a screened Coulomb pair potential is calculated as a function of composition and charge ratio. The potential energy obtained by a Lekner summation is minimized among a variety of candidate two-dimensional crystals. A wealth of different stable crystal structures is identified including A, B, AB_2, A_2B, AB_4 *structures [*A *(*B*) particles correspond to large (small) charge.] Their elementary cells consist of triangular, square or rhombic lattices of the* A *particles with a basis comprising various structures of* A *and* B *particles. For small charge asymmetry there are no intermediate crystals besides the pure* A *and* B *triangular crystals. The predicted structures are detectable in experiments on confined mixtures of like-charge colloids or dusty plasma sheets.*

1.1 Introduction

Two-component mixtures in general exhibit much richer crystallization phenomena and polymorphism than their one-component counterparts [42] as witnessed by a huge variety of possible stable binary crystals, e.g. for binary hard sphere systems [43–46]. How the whole crystal phase behavior in mixtures depends on the interparticle interactions is far from being understood even in equilibrium [47, 48]. This is true also in two spatial dimensions where the number of Bravais lattices is smaller than in three dimensions. Binary mixtures in two dimensions have been studied for hard disks [15] and a complex diagram of close packing was obtained as a function of their diameter ratio. More recently, a two-dimensional binary mixture

---

[1] This chapter was published by L. Assoud, R. Messina, and H. Löwen in *J. Chem. Phys.* *129* (2008).

with soft interactions was considered, [13] namely that for parallel dipoles where the pair potential scales with the inverse cube of the interparticle separation. A variant of this model has been considered in Ref. [49]. Such systems can be realized in granular matter [50] and in magnetic colloidal suspensions confined to an air-water interface [51]. Again, as a function of the ratio of dipole moments of the two species, a complex phase diagram of stable binary crystals was obtained that qualitatively differs from the hard disk case [15]. In particular for low asymmetries, the hard disk system shows a complete separation into pure A and B triangular crystals [15] while the soft dipolar systems possesses two stable mixed crystals as well with stoechiometric ratio A_2B and AB_2 [13]. These differences show that the topology of the phase diagrams depend on details of the interactions and there is certainly a need to understand this dependence in more detail.

In this paper, we consider a two-dimensional binary system of Yukawa point-like particles, i.e. the pair interaction potential $V(r)$ between the particles is a screened Coulomb interaction $\propto \exp(-\kappa r)/r$ where κ is the screening constant (or the inverse screening length). This repulsive potential interpolates between the case of hard disks (as obtained in the limit of high κ) and the unscreened Coulomb case (as obtained for $\kappa = 0$). The latter limit, $V(r) \propto 1/r$ is even softer than the dipolar case where $V(r) \propto 1/r^3$. The two components are defined by two different charges, i.e. different prefactors in front of the Yukawa interaction. In previous works, such a classical binary mixture with Yukawa interactions in three-dimensions has been used as a model to study mixing rules [52], effective forces [53], fluid-fluid phase separation [54–56], dynamical correlations [57, 58] and transport properties [59]. Likewise the pure (one-component) Yukawa system was also studied in two-spatial dimensions for fluid structure [60–63], dynamics [64–67] and transport properties [68]. Binary mixtures of Yukawa particles in two dimensions have also been studied for fluid structure [69], adsorption [70], interfaces [71] and transport [72].

The Yukawa potential is a good description for an effective pair interaction in *charged colloidal suspensions* [17] and in *dusty plasmas* [18], both for one component systems and mixtures. Here the microions establish a responding neutralizing background and they only enter via a Debye screening length and any microscopic details (as manifested e.g. in the Hofmeister series) are neglected. In fact, highly charged colloidal suspensions can be confined between highly charged parallel glass plates [19–21] which restricts their motion practically to two dimensions. As in three dimensions, the Debye-Hückel screened Coulomb interaction is a reasonable model for confined charged colloids [73, 74]. Crystallization of binary charged colloids has been studied experimentally in the bulk. For instance, the phase diagram for oppositely charged colloids can be found in Refs [75, 76]. A crystalline monolayer has also been realized experimentally for a confined binary mixture of like charged colloids (see Fig. 1 in Ref. [77])[2]. Similar studies exist also for sterically-stabilized [78] and

---

[2] However, intrinsic charge polydispersity has to be small enough in order to keep the charge distribution bimodal.

magnetic colloids [29]. On the other hand, sheets of highly charged dust particles in plasmas (so-called complex plasmas) can also be confined to two dimensions, e.g. by levitating electric fields. The interaction between the dust particles is again screened such that a Yukawa model is appropriate [18, 79, 80]. Highly charged microspheres suspended in a plasma settled in a horizontal monolayer were studied experimentally and compared to a two-dimensional Yukawa model [81–83]. There is no principle problem in studying binary mixtures of dust particles but a concrete realization in an experiments still has to be performed as well. Finally, another possible realization of the binary charged Yukawa system might be in two-component Langmuir-Blodgett films [84–86].

Apart from its important realizations, the major motivation for our studies is to understand the interplay between the interparticle interaction and the stability of different two-dimensional crystal lattices. A control of colloidal composite lattices may lead to new photonic crystals [87] to molecular-sieves [88] and to micro- and nano-filters with desired porosity [89]. The electric properties of a nanocrystal depend on its superlattice structure [90]. For these type of applications, it is crucial to understand the various stable lattice types in binary mixtures.

For the two-component two-dimensional Yukawa mixture, we obtain the full phase diagram at zero-temperature as a function of the charge asymmetry using lattice sums. As a result, we find a variety of different stable composite lattices. They include A, B, AB_2, A_2B, AB_4 structures. Their elementary cells consist of (equilateral) triangular, square and rhombic lattices of the big particles. These are highly decorated by a basis involving either A particles alone or both B and A particles. The topology of the resulting phase diagram differs qualitatively from that of hard disk mixtures [15] and dipoles [13].

The paper is organized as follows: In Sec. II the model is described and possible candidate structures for crystal lattices in two dimensions are proposed. Results for the thermodynamics and for the phase diagrams are presented in Sec. III. We conclude finally in Sec. IV.

1.2 Model

The model used in our study is a binary mixture of (repulsive) charged particles made up of two species denoted as A and B. Each component A and B is characterized by its charge valency Z_A and Z_B, respectively. These point particles are confined to a two-dimensional plane, and interact via a Yukawa pair potential. Introducing the charge ratio $Z = Z_B/Z_A$[3], the pair interaction potentials between two A particles,

---

[3] There is a trivial $Z \leftrightarrow 1/Z$ symmetry upon which one can safely reduce the phase diagram to $Z > 1$.

an A- and a B-particle, and two B-particles at distance r are

$$\begin{aligned} V_{AA}(r) &= \kappa V_0 \varphi(r), \quad V_{AB}(r) = \kappa V_0 Z \varphi(r), \\ V_{BB}(r) &= \kappa V_0 Z^2 \varphi(r), \end{aligned} \tag{1.1}$$

respectively. The dimensionless function $\varphi(r)$ is given by

$$\varphi(r) = \frac{\exp(-\kappa r)}{\kappa r}, \tag{1.2}$$

where the energy amplitude $V_0\kappa$ sets the energy scale. In Debye-Hückel theory, the prefactor reads as $V_0 = {Z_A}^2/\epsilon$ where ϵ is the dielectric permittivity of the solvent ($\epsilon = 1$ for the dusty plasma). Typically [91, 92], Z_A is of the order of $100 - 100000$ elementary charges e such that $V(r)/k_BT$ at typical interparticle distances $r = 1/\kappa$ equals $Z_A^2 \kappa \lambda_B / e^2$. Typically, the Bjerrum length $\lambda_B = e^2/\epsilon k_B T$ is a few Angstroms at room temperature and the Debye screening length $1/\kappa$ is a micron, such that $V(r)/k_BT$ is much larger than unity for high charges Z_A. This justifies formally zero-temperature calculations for the Yukawa particles. On the other hand, the screening microions possess a finite temperature which enters in the inverse Debye screening length κ.

Our goal is to determine the stable crystalline structures adopted by the system at zero temperature. We consider a parallelogram as a primitive cell which contains n_A A-particles and n_B B-particles. This cell can be described geometrically by the two lattice vectors $\mathbf{a} = a(1, 0)$ and $\mathbf{b} = a\gamma(\cos\theta, \sin\theta)$, where θ is the angle between $\mathbf{a}$ and $\mathbf{b}$ and γ is the aspect ratio ($\gamma = |\mathbf{b}|/|\mathbf{a}|$). The position of a particle i (of species A) and that of a particle j (of species B) in the parallelogram is specified by the vectors $\mathbf{r}_{\mathrm{i}}^A = (x_i^A, y_i^A)$ and $\mathbf{r}_{\mathrm{j}}^B = (x_j^B, y_j^B)$, respectively. The total internal energy (per primitive cell) U has the form

$$\begin{aligned} U = \frac{1}{2} \sum_{J=A,B} \sum_{i,j=1}^{n_J} {\sum_{\mathbf{R}}}' V_{JJ}\left(\left|\mathbf{r}_i^J - \mathbf{r}_j^J + \mathbf{R}\right|\right) \\ + \sum_{i=1}^{n_A} \sum_{j=1}^{n_B} \sum_{\mathbf{R}} V_{AB}(\left|\mathbf{r}_i^A - \mathbf{r}_j^B + \mathbf{R}\right|), \end{aligned} \tag{1.3}$$

where $\mathbf{R} = k\mathbf{a} + l\mathbf{b}$ with k and l being integers. The sums over $\mathbf{R}$ in Eq. 1.3 run over all lattice cells where the prime indicates that for $\mathbf{R} = 0$ the terms with $i = j$ are to be omitted. In order to handle efficiently the long-range nature of the Yukawa interaction at moderate screening strength, we employed a Lekner-summation (see Appendix A).

We choose to work at prescribed pressure[4] p and zero temperature ($T = 0$). Hence, the corresponding thermodynamic potential is the Gibbs free energy G. Additionally, we consider interacting particles at composition $X := n_B/(n_A + n_B)$,

---

[4] For a confined colloidal suspension, p is the total lateral osmotic pressure of the colloids.

so that the (intensive) Gibbs free energy g per particle reads: $g = g(p, Z, X) = G/(n_A + n_B)$. At vanishing temperature, g is related to the internal energy per particle $u = U/(n_A + n_B)$ through $g = u + p/\rho$, where the pressure p is given by $p = \rho^2(\partial u/\partial \rho)|_{n_A,n_B}$, and $\rho = (n_A + n_B)/|\mathbf{a} \times \mathbf{b}|$ is the total particle density. The Gibbs free energy per particle g has been minimized with respect to γ, θ and the position of particles of species A and B within the primitive cell. In order to decrease the complexity of the energy landscape, we have limited the number of variables and considered the following candidates for our binary mixtures: A_4B, A_3B, A_2B, A_4B_2, A_3B_2, AB, A_2B_2, A_3B_3, A_2B_3, AB_2, A_2B_4, AB_3, AB_4 and AB_6. Note that crystalline alloys with chemical disorder which are stable due to mixing entropy are not considered here since our study is limited to zero temperature. For the AB_6 and A_3B_3 case we have only considered a triangular lattice formed by the A particles. An overview of the resulting stable crystalline phases can be found in Fig. 1.1. The corresponding nomenclature of the phase labeling is summarized and explained in Table 1.1. The crystalline structures are getting increasingly complex from top to bottom in Fig. 1.1 and Table 1.1. Pure triangular lattices [$\mathbf{T}(A)$ resp. $\mathbf{T}(B)$] and checkerboard structures with equal molarities [$\mathbf{S}(AB)$] are the simpler structures while more complex basic unit cells with a complicated basis are included as well.

1.3 Results

1.3.1 Thermodynamical properties

Gibbs free energy

We first would like to address the behavior of the reduced Gibbs free energy per particle $g^* \equiv g/(V_0\kappa)$ at prescribed charge ratio Z. The (*discrete*) profiles of g^* for different values of Z as a function of the composition X are depicted in Fig. 1.2. The different data points shown in Fig. 1.2 correspond to the phase (see Table 1.2) with the lowest energy at given composition and charge ratio. This does not necessarily imply that this particular phase is globally stable, see our discussion below. The qualitative trends of g^* are not affected upon varying the pressure. In the following we introduce a reduced pressure $p^* = p/(V_0\kappa^3)$.

At given composition X, Fig. 1.2 shows that g^* decreases with decreasing charge ratio Z. Recalling that $g^* = u^* + p^*/\rho^*$ [with $u^* \equiv u/(V_0\kappa)$], this feature can be discussed in terms of u^* and ρ^*. More precisely, at prescribed value for X, the system has to lower its density such as to keep the pressure constant when Z is enlarged. This clearly explains why the term in p^*/ρ^* increases here with growing Z at fixed X. What is less straightforward to clarify, is the resulting behavior of u^* (with respect to Z and ρ^*) which can only be specified after the explicit numerical calculations.

The other general trend revealed in Fig. 1.2 is that g^* decreases with growing composition X at prescribed charge ratio Z. This feature is fully consistent with the

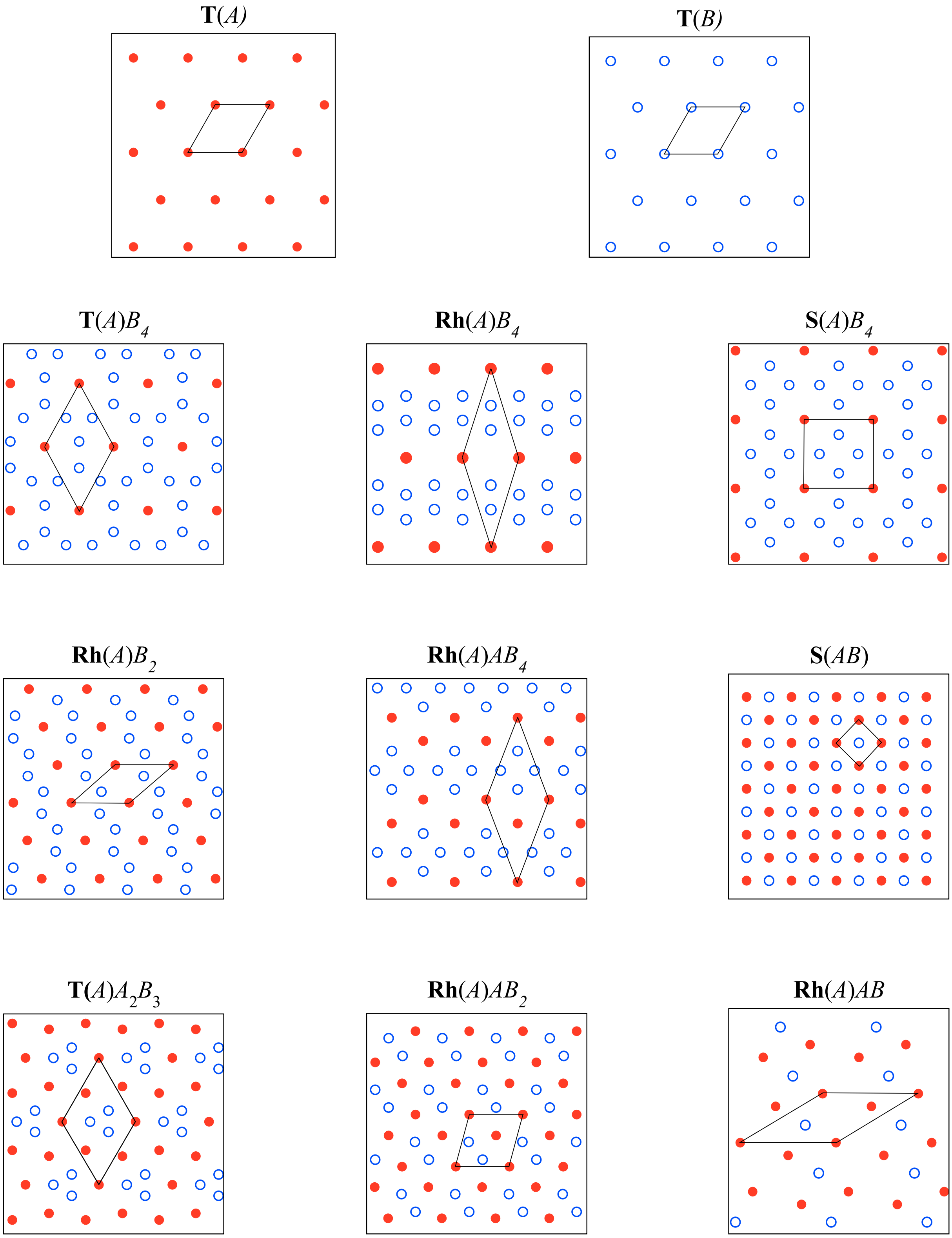

T(A)

T(B)

T(A)B_4

Rh(A)B_4

S(A)B_4

Rh(A)B_2

Rh(A)AB_4

S(AB)

T(A)A_2B_3

Rh(A)AB_2

Rh(A)AB

Figure 1.1: The stable binary crystal structures and their primitive cells. The discs (open circles) correspond to A (B) particles.

Table 1.1: The stable phases with their Bravais lattice and their basis.

Phase	Bravais lattice [basis]
$\mathbf{T}(A)$	Triangular for A [one A particle]
$\mathbf{T}(B)$	Triangular for B [one B particle]
$\mathbf{S}(AB)$	Square for A and B together [one A and one B particles]
$\mathbf{S}(A)B_n$	Square for A [one A and n B particles]
$\mathbf{Rh}(A)A_mB_n$	Rhombic for A [$(m+1)$ A and n B particles]
$\mathbf{T}(A)A_mB_n$	Triangular for A [$(m+1)$ A and n B particles]

idea that upon enlarging X, the proportion of *weakly* charged B-particles increases accordingly, so that to keep the pressure constant the system has to increase its density and therefore the term $1/\rho^*$ in g^* decreases. Again, the behavior of u^* is not trivial à priori.

Phase coexistence

In this part, we explain how a phase coexistence sets in. The onset of phase coexistence is based on the common tangent construction also called Maxwell construction. At coexistence, two conditions must be fulfilled: (i) the pressure p^* needs to be equal for each phase (in our situation this is always guaranteed since we are working at prescribed pressure) and (ii) the chemical potential for any component must be the same for the two coexisting phases. If we denote by $\mu_i^{\pi_j}$, with $i = A, B$ and $j = 1, 2$ the chemical potential associated to particles of i-species for phase π_j, then the thermodynamical condition (ii) can be mathematically expressed as: $\mu_A^{\pi_1} = \mu_A^{\pi_2}$ and $\mu_B^{\pi_1} = \mu_B^{\pi_2}$.

The geometrical interpretation of this latter thermodynamical condition combined with that of the minimization of g^* is exemplified in Fig. 1.3. Thereby, we have plotted $\Delta g^*(X) = g^*(X) - [(1-X)g_A^* + Xg_B^*]$, where $g_A^* = g^*(X=0)$ and $g_B^* = g^*(X=1)$. The common tangent construction for crystalline phases consists merely of excluding all metastable phases in the discrete profile of $\Delta g^*(X)$. For the examples chosen in Fig. 1.3 it turns out that for $Z = 0.7$ all mixtures are unstable so that the resulting equilibrium system will always split into a pure A and pure B triangular crystals. On the other hand, when $Z = 0.3$, three stable mixtures for $X = 1/2, 2/3$ and $4/5$ set in which are explicitly mentioned in Figure 3. They are all hit by the two double tangents. In total, there are four pieces of common tangents shown in Figure 3 (lower part) for $Z = 0.3$ as a dashed line.

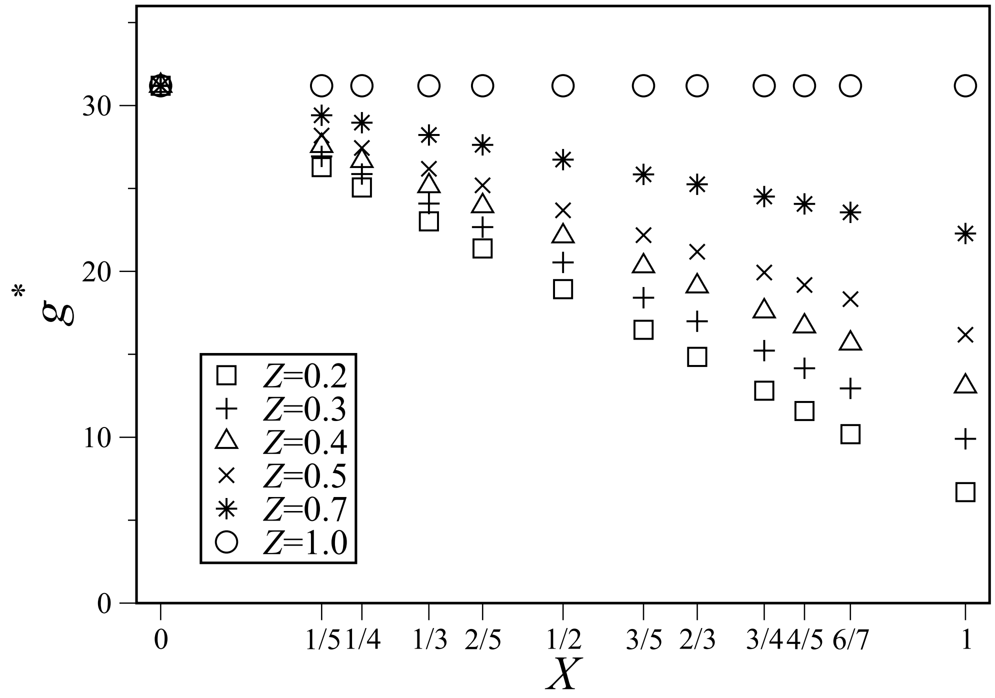

Figure 1.2: Reduced Gibbs free energy g^* as a function of the composition X for various charge ratios Z at prescribed reduced pressure $p^* = 100$. The different data points shown correspond to the phase with the lowest energy at given composition and charge ratio. The case $Z = 1$ corresponds to the pure phase $\mathbf{T}(A)$ (or equivalently $\mathbf{T}(B)$). All the other phases are gathered in Table 1.2.

Table 1.2: The phases with the lowest Gibbs free energy g^* appearing in Fig. 1.2. The labels **Re** and **Pa** correspond to rectangular and parallelogram shaped primitive cells.

X Z	0.2	0.3	0.4	0.5	0.7
0	$\mathbf{T}(A)$	$\mathbf{T}(A)$	$\mathbf{T}(A)$	$\mathbf{T}(A)$	$\mathbf{T}(A)$
1/5	$\mathbf{Rh}(A)A_3B$	$\mathbf{Rh}(A)A_3B$	$\mathbf{Rh}(A)A_3B$	$\mathbf{Rh}(A)A_3B$	$\mathbf{Rh}(A)A_3B$
1/4	$\mathbf{Re}(A)A_2B$	$\mathbf{Re}(A)A_2B$	$\mathbf{Re}(A)A_2B$	$\mathbf{Re}(A)A_2B$	$\mathbf{Re}(A)A_2B$
1/3	$\mathbf{Rh}(A)AB$	$\mathbf{Re}(A)A_3B_2$	$\mathbf{Pa}(A)A_3B_2$	$\mathbf{Pa}(A)A_3B_2$	$\mathbf{T}(A_2B)$
2/5	$\mathbf{Rh}(A)A_2B_2$	$\mathbf{Re}(A)A_2B_2$	$\mathbf{Pa}(A)A_2B_2$	$\mathbf{Pa}(A)A_2B_2$	$\mathbf{Rh}(A)A_2B_2$
1/2	$\mathbf{S}(AB)$	$\mathbf{Rh}(A)AB_2$	$\mathbf{Rh}(A)AB_2$	$\mathbf{Rh}(A)AB_2$	$\mathbf{Re}(A)AB_2$
3/5	$\mathbf{Re}(A)AB_3$	$\mathbf{Re}(A)AB_3$	$\mathbf{Pa}(A)AB_3$	$\mathbf{Pa}(A)AB_3$	$\mathbf{Rh}(A)AB_3$
2/3	$\mathbf{Rh}(A)AB_2$	$\mathbf{Rh}(A)AB_2$	$\mathbf{Rh}(A)AB_4$	$\mathbf{Rh}(A)AB_4$	$\mathbf{T}(AB_2)$
3/4	$\mathbf{Pa}(A)B_3$	$\mathbf{Re}(A)B_3$	$\mathbf{Re}(A)B_3$	$\mathbf{Re}(A)B_3$	$\mathbf{Re}(A)B_3$
4/5	$\mathbf{T}(A)B_4$	$\mathbf{Rh}(A)B_4$	$\mathbf{S}(A)B_4$	$\mathbf{S}(A)B_4$	$\mathbf{Rh}(A)B_4$
6/7	$\mathbf{T}(A)B_6$	$\mathbf{T}(A)B_6$	$\mathbf{T}(A)B_6$	$\mathbf{T}(A)B_6$	$\mathbf{T}(A)B_6$
1	$\mathbf{T}(B)$	$\mathbf{T}(B)$	$\mathbf{T}(B)$	$\mathbf{T}(B)$	$\mathbf{T}(B)$

Particle density

The reduced density ρ^* as a function of the charge ratio Z at different compositions X is sketched in Fig. 1.4. At given composition X, the density decreases monotonically with Z, see Fig. 1.4. This effect can be simply explained as follows: Upon increasing Z the repulsive $A-B$ and $B-B$ pair interactions increase accordingly, so that to keep the pressure fixed the system has to decrease its density. Moreover, at prescribed charge ratio, Fig. 1.4 indicates that the density increases with the composition. This feature can also be explained with simple physics: Upon enlarging the composition X, the proportion of *weakly* charged B-particles increases accordingly, so that to keep the pressure constant the system has to increase its density. This particle density behavior is important to better understand later the phase diagram which is shown for prescribed pressure.

1.3.2 Phase diagram

The ultimate phase diagrams in the (Z, X) plane has been obtained by employing the Maxwell construction. To allow an easier comparison with earlier works, [13,15] we have chosen the same y-axis, namely here the composition X. We recall here that the both dimensionless quantities, namely the charge ratio Z as well as the composition X, can vary between zero and unity. A low charge ratio (i.e., Z is close to zero) indicates a strong charge asymmetry, whereas a high charge ration (i.e., Z is close to unity) represents a large charge symmetry or equivalently a weak

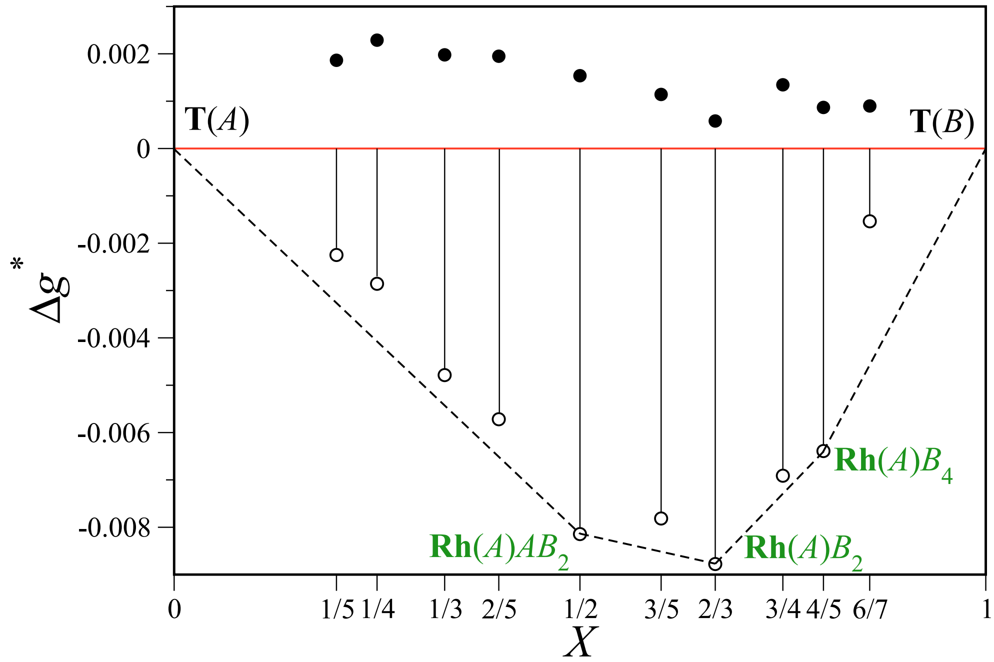

Figure 1.3: Common tangent construction for crystalline phases at prescribed reduced pressure $p^* = 100$. The filled (open) circles correspond to $Z = 0.7$ ($Z = 0.3$). The stable phases are indicated explicitly.

charge asymmetry. Given the fact that the phase behavior is getting increasingly complicated upon lowering Z, involving a huge basket of candidates, we only present results starting from $Z = 0.2$. Furthermore, in contrast to situations where the pair potential can be described as a power law of the separation distance (as it was the case in our previous work on dipolar mixtures, [13]) the phase diagram becomes pressure dependent for Yukawa systems. To capture this feature, we present results at three well distinct pressures, namely $p^* \equiv p/(V_0\kappa^3) = 0.01, 1$ and 100.

The phase diagrams in the (Z, X) plane for the three reduced pressures $p^* = 0.01, 1$ and 100 are depicted in Fig. 1.5(a), Fig. 1.5(b), and Fig. 1.5(c), respectively.

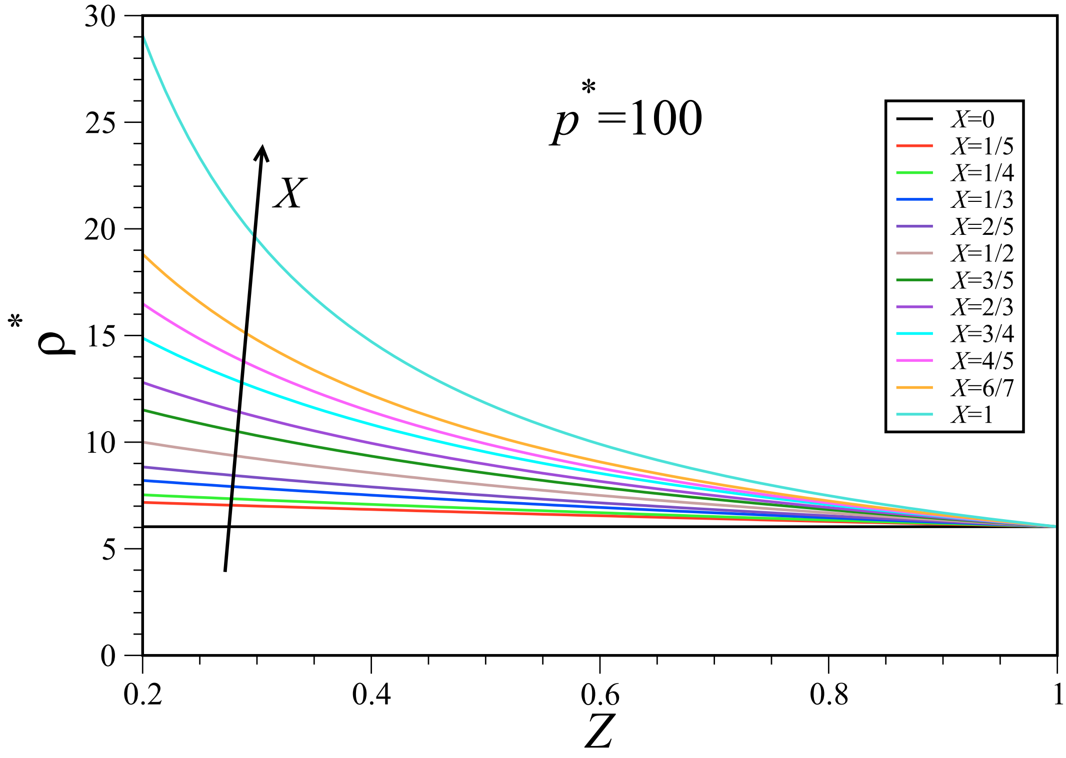

Figure 1.4: Reduced density ρ^* (prior the Maxwell construction) as a function of the charge ratio Z for various compositions X at prescribed reduced pressure $p^* = 100$. The arrow indicates growing X.

Weak charge asymmetry

Let us first focus our discussion on the apparently simple phase behavior reported at weak charge asymmetry (here roughly $Z \gtrsim 0.5$, see Fig. 1.5). Thereby, the system phase separates into a pure A and a pure B triangular crystalline phase (see also

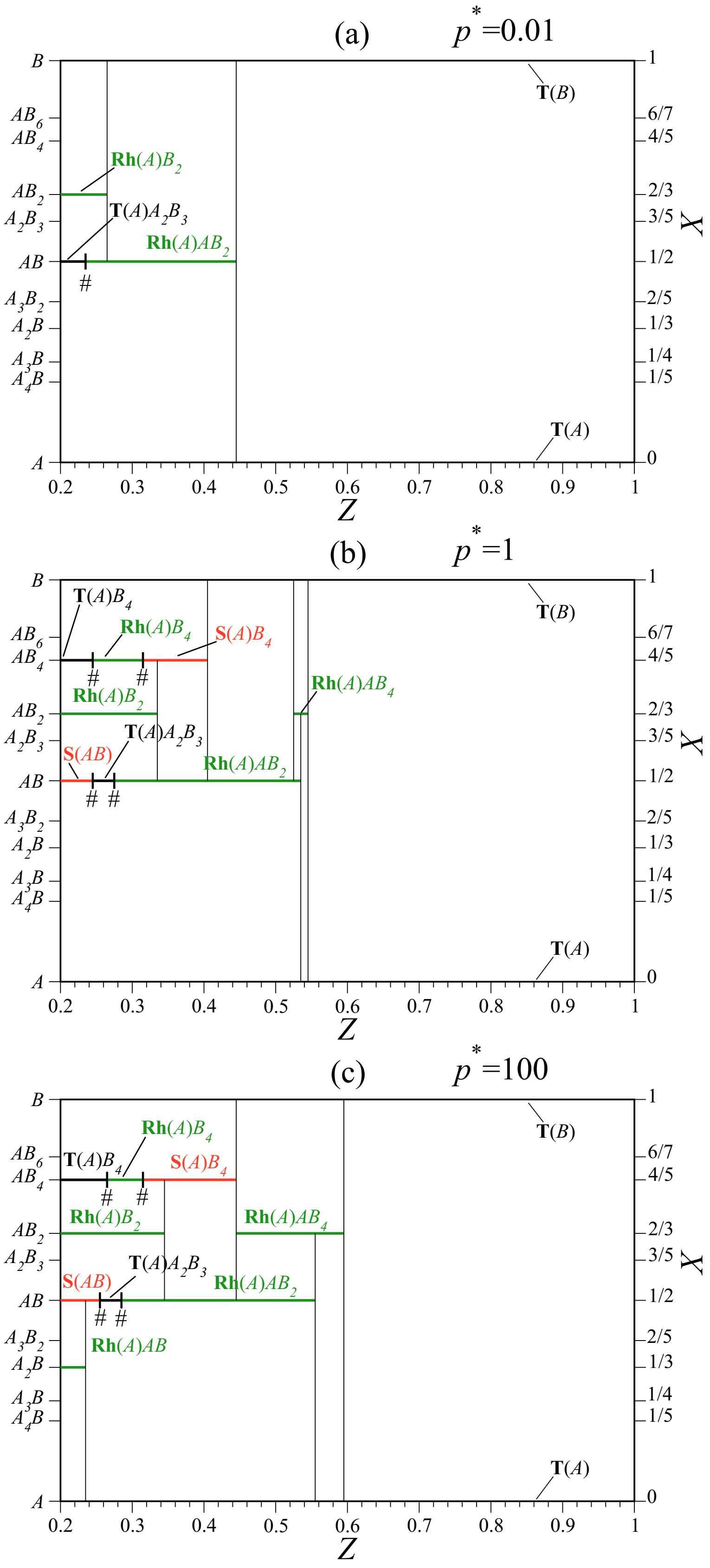

Figure 1.5: The phase diagram in the (Z, X) plane of charge asymmetry and composition at $T = 0$ for an effective pressure (a) $p^* = 0.01$, (b) $p^* = 1$, (c) $p^* = 100$. The symbol # denotes a discontinuous transition. The y-axis is represented by two equivalent scales: The left side indicates the phase symbols whereas the right one shows the corresponding value of the composition.

Fig. 1.1). This triangular structure obviously corresponds to the single-component ground-state.

What is now less obvious, still in the regime of weak charge asymmetry, is the phase separation reported in Fig. 1.5(c) for $p^* = 100$. Recently, we have shown for dipolar binary mixtures, [13] whose pair potential is governed by $1/r^3$, that, at weak dipolar asymmetry (the analogous quantity to the charge ratio in our present study), the *stable mixtures* A_2B and AB_2 (who are globally triangular) set in. This phase behavior contrasts therefore strongly with that reported here for Yukawa mixtures, see Fig. 1.5(c). Given the fact that at weak screening the Yukawa pair potential is well approximated by a $1/r$ dependence, which is even softer than $1/r^3$, it is legitimate to expect stable mixtures in the regime of weak screening and charge asymmetry. In order to check this idea we have performed additional calculations at $p^* = 10^{10}$ with $Z = 0.99$ leading to reduced screening strengths of the order of 10^{-2}. Those values for κ^* turn out to be still too large to recover the phase behavior found at $1/r^3$-pair interactions [13]. The consideration of even much smaller screening strengths (say roughly of the order of 10^{-7}) are numerically not tractable within reasonable CPU time. Unfortunately, the implementation of a direct Lekner and/or Ewald sum for the $1/r$-pair interactions is delicate at *prescribed pressure*, since the lack of electroneutrality involves the presence of an artificial homogeneous neutralizing background which is thermodynamically only consistent at *prescribed density* [93]. Consequently, although we have a strong intuition about the stability of mixtures at weak charge asymmetry and screening, we can not prove it here on computational basis.

Large charge asymmetry

We now address the more complicated phase behavior reported at strong charge asymmetry, see Fig. 1.5 with $Z \lesssim 0.5$. As a clear general trend, it is found that the number of stable phases increases with growing pressure. This feature is in agreement with the idea that mixing is favored upon softening the pair potential.

A common and remarkable feature in this regime of strong charge asymmetry (see Fig. 1.5) is the imposing stability of equal composition $X = 1/2$. This feature was also reported for dipolar mixtures [13]. Let us discuss the behavior at $X = 1/2$ in more detail. In fact, the following cascade $\mathbf{S}(AB) \rightarrow \mathbf{T}(A)A_2B_3 \rightarrow \mathbf{Rh}(A)AB_2$ is found upon increasing Z, see Fig. 1.5 and Fig. 1.1 for the corresponding structures. Thereby, the transitions $\mathbf{S}(AB) \rightarrow \mathbf{T}(A)A_2B_3$ and $\mathbf{T}(A)A_2B_3 \rightarrow \mathbf{Rh}(A)AB_2$ are discontinuous, see Fig. 1.5. These discontinuous transitions stem merely from the lattice-geometry incompatibility among the phases, see Fig. 1.1. Note that, for $p^* = 0.01$ shown in Fig. 1.5(a), the stability of the square phase $\mathbf{S}(AB)$ occurs for values of Z smaller than 0.2 that are not shown here.

In order to compare the phase behavior with that of hard disk mixtures, we have

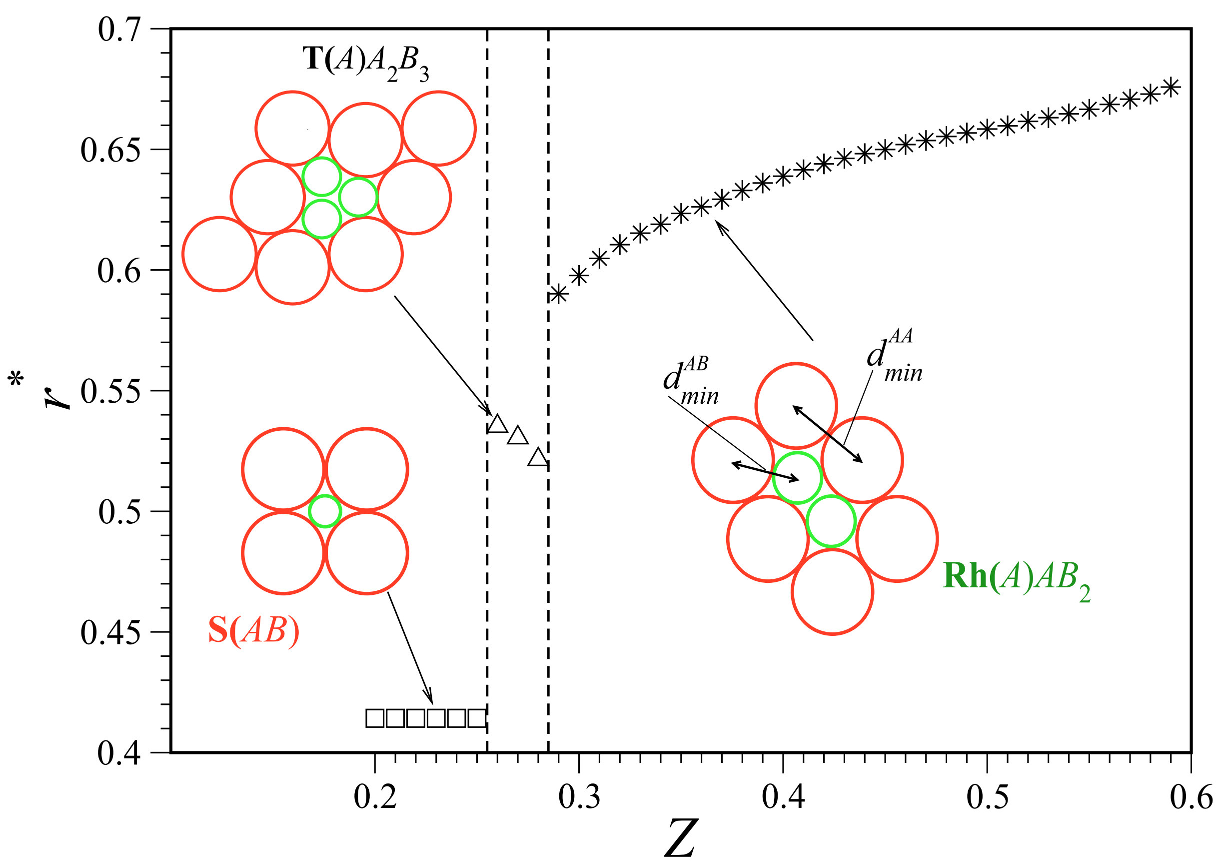

Figure 1.6: Geometrical order parameter $r^* = (2d_{min}^{AB} - d_{min}^{AA})/d_{min}^{AA}$ as a function of the charge ratio Z for the given composition $X = 1/2$ at prescribed reduced pressure $p^* = 100$. The equivalent stable hard disk systems are sketched as well as the distances d_{min}^{AB} and d_{min}^{AA} for the $\mathbf{Rh}(A)AB_2$ phase.

considered the following dimensionless geometrical order parameter:

$$r^* \equiv \frac{2d_{min}^{AB} - d_{min}^{AA}}{d_{min}^{AA}} \quad (r \leq 1), \tag{1.4}$$

where d_{min}^{AB} corresponds to the shortest distance between A- and B-particles whereas d_{min}^{AA} stands for that between A-particles within the Wigner-Seitz cell (see Fig. 1.6). Physically, this quantity r^* is the size-ratio between big and small particles in a (packed) binary hard disk crystal [15], i.e. for touching configurations. The profile of r^* along the cascade $\mathbf{S}(AB) \to \mathbf{T}(A)A_2B_3 \to \mathbf{Rh}(A)AB_2$ depicted in Fig. 1.5(c) is sketched in Fig. 1.6 as a function of Z. As expected, r^* undergoes two jumps at $Z = 0.255$ and $Z = 0.285$ which are the signatures of discontinuous transitions. Fig. 1.6 reveals that r^* is *growing* with Z except for the tiny interval where the $\mathbf{T}(A)A_2B_3$ phase is stable. This demonstrates an interesting analogy between the charge ratio Z in like charged binary mixtures and the size ratio r^* in hard disk binary mixtures consistent with earlier investigations where size-polydispersity was mapped onto charge polydispersity [94] and a strong correlation between size and charge polydispersity was found. In fact, for hard-disk mixtures there is also a first-order transition from the $\mathbf{S}(AB)$ directly to the $\mathbf{Rh}(A)AB_2$ phase at a size asymmetry between 0.4 and 0.5 [15]. This is the analogy of the start and end of the cascade $\mathbf{S}(AB) \to \mathbf{T}(A)A_2B_3 \to \mathbf{Rh}(A)AB_2$. It is interesting that the hard-disk transition occurs at similar size asymmetries as indicated on the y axis of Fig. 1.6. However, in our case, the additional structure $\mathbf{T}(A)A_2B_3$ (with a decreasing r^*) intervenes.

1.4 Concluding remarks

In conclusion we have determined the ground-state (i.e. zero-temperature) phase diagram for a two-component Yukawa monolayer at various pressures for arbitrary compositions and a broad range of charge asymmetries. Among a big number of candidate phases, a wealth of different composite lattices has been found to be stable. The larger the charge asymmetry, the more complex is the phase diagram. At low asymmetry the system shows demixing into pure A and B crystals similar to hard disks but different from the soft inverse cube interaction valid for dipoles. At higher asymmetries and same composition of high-charge and low-charge particles, there are two first-order transitions between three different crystalline structure with incompatible symmetry. The latter transitions were compared with the corresponding hard-disk behavior. The results are in principle detectable in binary mixtures of charged colloids confined between two charged plates [77] or levitated dusty plasma sheets [95].

It would be interesting to study the effect of finite temperature. We expect that the topology of the phase diagram does not change upon gently increasing the temperature though this could change close to melting. In this respect, colloid-polymer mixtures are useful model systems where the concentration of non-adsorbing polymers plays the role of inverse temperature, see e.g. Refs. [96,97].

When cooling a two-component fluid down, glass formation in the binary systems at finite temperature may be a fascinating topic as well [98] to be studied in the future. In fact, it has been speculated that the underlying crystallization into the stable crystal lattices may control vitrification [99] and therefore our findings are directly relevant for the structure of glasses.

We thank T. Palberg and H. Tanaka for helpful discussions. This work was supported by the DFG via the SFB TR6 (project D1).

1.5 Lekner sums for Yukawa interactions in two dimensional systems

We consider a primitive cell in the shape of a parallelogram, which contains a set of $n = n_A + n_B$ particles interacting via Yukawa potentials. The parallelogram repeated in the xy plane gives a 2-dimensional lattice, and can be described by two lattice vectors $\mathbf{a} = (a_x, 0)$ and $\mathbf{b} = (b_x, b_y)$. In the parallelogram, the position of a charge valency Z_i is defined by $\mathbf{r}_i = (x_i, y_i)$.

The total interaction energy per cell is given by

$$\frac{U}{V_0} = \frac{1}{2}\sum_{i=1}^{n}\sum_{j\neq 1}^{n} Z_i Z_j \Phi(\mathbf{r}_{ij}) + \frac{1}{2}\sum_{i=1}^{n} Z_i^2 \Phi_0 \tag{1.5}$$

with

$$\Phi(\mathbf{r}) = \sum_{\mathbf{R}} \frac{\exp(-\kappa|\mathbf{r}+\mathbf{R}|)}{|\mathbf{r}+\mathbf{R}|} \quad \text{and} \quad \Phi_0 = \sum_{\mathbf{R}\neq 0} \frac{\exp(-\kappa|\mathbf{R}|)}{|\mathbf{R}|}, \tag{1.6}$$

where

$$|\mathbf{r}+\mathbf{R}| = \sqrt{(x + a_x l + b_x m)^2 + (y + b_y m)^2} \quad \text{and} \quad |\mathbf{R}| = \sqrt{(a_x l + b_x m)^2 + (b_y m)^2}.$$

Here $\mathbf{R} = l\mathbf{a} + m\mathbf{b}$ with l and m being integers. The slowly convergent sums over lattice sites (Eq. 1.6) can not be efficiently used in a numerical calculation, so that we will transform them into rapidly convergent forms using a Lekner Method [100,101]. With the help of the following integral representation

$$\frac{\exp(-\kappa|\mathbf{r}+\mathbf{R}|)}{|\mathbf{r}+\mathbf{R}|} = \frac{1}{\sqrt{\pi}}\int_0^\infty \frac{dt}{\sqrt{t}} \exp\,(-\frac{\kappa^2}{4t} - |\mathbf{r}+\mathbf{R}|^2 t), \tag{1.7}$$

we obtain

$$\Phi(\mathbf{r}) = \frac{1}{\sqrt{\pi}}\int_0^\infty \frac{dt}{\sqrt{t}} \left\{ \exp(-\frac{\kappa^2}{4t}) \sum_{m=-\infty}^{\infty}\sum_{l=-\infty}^{\infty} \exp\left[-(y + m b_y)^2 t\right] \exp\left[-\left(\frac{x}{a_x} + l + m\frac{b_x}{a_x}\right)^2 a_x^2 t\right] \right\}. \tag{1.8}$$

Now, to get further, we apply a 1-dimensional Poisson summation

$$\sum_{l=-\infty}^{\infty} \exp\left[-(\alpha+\beta l)^2 t\right] = \frac{\sqrt{\pi}}{\beta\sqrt{t}} \sum_{k=-\infty}^{\infty} \exp\left(i2\pi k\frac{\alpha}{\beta}\right) \exp\left(-\frac{\pi^2 k^2}{\beta^2}\frac{1}{t}\right), \tag{1.9}$$

which provides

$$\sum_{l=-\infty}^{+\infty} \exp\left[-(\frac{x}{a_x}+l+m\frac{b_x}{a_x})^2 a_x^2 t)\right] = \frac{1}{|a_x|}\sqrt{\frac{\pi}{t}}\left[1+2\sum_{k=1}^{+\infty}\cos\left[2\pi k\left(\frac{x}{a_x}+m\frac{b_x}{a_x}\right)\right]\exp\left(-\pi^2 k^2/a_x^2 t\right)\right]. \tag{1.10}$$

Inserting Eq. (1.10) into Eq. (1.8) yields:

$$\begin{aligned} \Phi(\mathbf{r}) &= \frac{1}{|a_x|}\sum_{m=-\infty}^{\infty}\int_0^{\infty}\frac{dt}{t}\exp\left[-\frac{\kappa^2}{4t}-(y+mb_y)^2 t\right] \\ &+\frac{2}{|a_x|}\sum_{k=1}^{+\infty}\sum_{m=-\infty}^{+\infty}\cos\left[2\pi k\left(\frac{x}{a_x}+m\frac{b_x}{a_x}\right)\right] \\ &\times\int_0^{\infty}\frac{dt}{t}\exp\left[-\left(\kappa^2+\frac{4\pi^2k^2}{a_x^2}\right)\frac{1}{4t}-(y+mb_y)^2 t\right] \end{aligned} \tag{1.11}$$

Now, taking into account the following relation

$$\int_0^{\infty}\frac{dt}{t}\exp\left(-\frac{B^2}{4t}-C^2 t\right) = 2K_0(BC) \tag{1.12}$$

where K_0 is the zeroth order modified Bessel function of the second kind. The final expression for $\Phi(\mathbf{r})$ reads:

$$\begin{aligned} \Phi(\mathbf{r}) &= \frac{2}{|a_x|}\sum_{m=-\infty}^{+\infty}K_0\left(\kappa|y+mb_y|\right) \\ &+\frac{4}{|a_x|}\sum_{k=1}^{\infty}\sum_{m=-\infty}^{+\infty}\cos\left[2\pi\left(\frac{x}{a_x}+m\frac{bx}{a_x}\right)\right] \\ &\times K_0\left[|y+mb_y|\sqrt{\kappa^2+\frac{4\pi^2k^2}{a_x^2}}\right] \qquad \text{for } y\neq 0 \end{aligned} \tag{1.13}$$

and the “self” contribution Φ_0

$$\begin{aligned} \Phi_0 &= \frac{4}{|a_x|}\sum_{m=1}^{\infty}K_0(\kappa m b_y) \\ &+\frac{8}{|a_x|}\sum_{k=1}^{\infty}\sum_{m=1}^{\infty}\cos\left(2\pi k m\frac{bx}{a_x}\right)K_0\left[mb_y\sqrt{\kappa^2+\frac{4\pi^2k^2}{a_x^2}}\right] \\ &-\frac{2}{|a_x|}\ln\left[1-\exp(-\kappa a_x)\right] \end{aligned} \tag{1.14}$$

In the limit of a rectangular based cell, i.e setting $b_x = 0$, one obtains the formulas for the cross and self-energies that are identical to those derived in [101] with $z = 0$.

The sums in Eqs. (1.13) and (1.14) are truncated (i.e., the criterion of convergence is realized) when the Bessel function values are smaller than 10^{-12}. This typically leads to a relative error in the energy that is smaller than 10^{-11}. In the case of double sums the cut-offs are identical, i.e., $k_c = m_c$, such that all terms with $k \leq k_c$ and $|m| \leq m_c$ are included in the sums.

Chapter 2

Stable crystalline lattices in two-dimensional binary mixtures of dipolar particles [1]

Abstract

The phase diagram of binary mixtures of particles interacting via a pair potential of parallel dipoles is computed at zero temperature as a function of composition and the ratio of their magnetic susceptibilities. Using lattice sums, a rich variety of different stable crystalline structures is identified including A_mB_n *structures. [*A *(*B*) particles correspond to large (small) dipolar moments.] Their elementary cells consist of triangular, square, rectangular or rhombic lattices of the* A *particles with a basis comprising various structures of* A *and* B *particles. For small (dipolar) asymmetry there are intermediate* AB_2 *and* A_2B *crystals besides the pure* A *and* B *triangular crystals. These structures are detectable in experiments on granular and colloidal matter.*

While the freezing transition and the corresponding crystal lattice in one-component systems is well-understood by now [102, 103], binary mixtures of two different particle species exhibits a much richer possibility of different solid phases. For example, while a one-component hard sphere system freezes into the close-packed face-centered-cubic lattice [43], binary hard sphere mixtures exhibit a huge variety of close-packed structures depending on their diameter ratio. These structures include AB_n superlattices, where A are the large and B the small spheres, with $n = 1, 2, 5, 6, 13$. These structures were found in theoretical calculations [44], computer simulations [45, 104] and in real-space experiments on sterically stabilized colloidal suspensions [46, 105]. Much less is known for soft repulsive interparticle interactions; most recent studies on crystallization include attractions and

---

[1] This chapter was published by L. Assoud, R. Messina, and H. Löwen in *Europhys. Lett. 80* (2007), 48001.

consider Lennard-Jones mixtures [106, 107] or oppositely charged colloidal particles [75, 76, 108].

In this letter we explore the phase diagram of a binary mixture interacting via a soft repulsive pair potential proportional to the inverse cube of the particle separation. Using lattice sums, we obtain the zero-temperature phase diagram as a function of composition and asymmetry, i.e. the ratio of the corresponding prefactors in the particle-particle interaction. Our motivation to do so is threefold:

i) First there is an urgent need to understand the effect of softness in general and in particular in two spatial dimensions. The case of hard interactions in two spatial dimensions, namely binary hard disks, has been obtained by Likos and Henley [15] for a large range of diameter ratios. A complex phase behavior is encountered and it is unknown how the phase behavior is affected and controlled by soft interactions.

ii) The model of dipolar particles considered in this letter is realized in quite different fields of physics. Dipolar *colloidal particles* can be realized by imposing a magnetic field [109]. In particular, our model is realized by micron-sized superparamagnetic colloidal particles which are confined to a planar water-air interface and exposed to an external magnetic field parallel to the surface normal [109–113]. The magnetic field induces a magnetic dipole moment on the particles whose magnitude is governed by the magnetic susceptibility. Hence their interaction potential scales like that between two parallel dipoles with the inverse cube of the particle distance. Binary mixtures of colloidal particles with different susceptibilities have been studied for colloidal dynamics [114], fluid clustering [29, 115], and the glass transition [27]. A complementary way to obtain dipolar colloidal particles is a fast alternating electric field which generates effective dipole moments in the colloidal particles [116]. This set-up has been applied for two-dimensional binary mixtures in Ref. [117]. In *granular matter*, the model has been realized by mixing millimeter-sized steel and brass spheres [50] which are placed on a horizontal plate and exposed to a vertical magnetic field such that the repulsive dipole-dipole interaction is the leading term. Stable triangular AB_2 crystalline lattice were found [50]. Layers of *dusty plasmas* involve particles whose interactions can be dominated by that of dipoles [118–120]. Other situations where two-dimensional mixtures of parallel dipoles are relevant concern *amphiphiles* (confined to a monomolecular film at an air-water interface [121]), *binary monolayers* [122–124], *ferrofluid* monolayers [125] exposed to a perpendicular magnetic field, or thin films of *molecular* mixtures (e.g. of boron nitride and hydrocarbon molecules) with a large permanent dipole moment [126]. Hence, in principle, our results can be directly compared to various experiments of (classical) dipolar particles with quite different size in quite different set-ups.

iii) It is important to understand the different crystalline sub-structures in detail, since a control of the colloidal composite lattices may lead to new optical band-gap materials (so-called photonic crystals) [87] to molecular-sieves [88] and to micro- and nano-filters with desired porosity [89]. Nano-sieves and filters can be constructed on a colloidal monolayer confined at interfaces [89]. Their porosity is directly coupled to their crystalline structure. For these applications, it is mandatory to understand the different stable lattice types which occur in binary mixtures.

As a result, we find a variety of different stable composite lattices. They include A_mB_n structures with, for instance, $n = 1, 2, 4, 6$ for $m = 1$. Their elementary cells consist of (equilateral) triangular, square, rectangular and rhombic lattices of the A particles. These are highly decorated by a basis involving either B particles alone or both B and A particles. The topology of the resulting phase diagram differs qualitatively from that of hard disk mixtures [15]. For small (dipolar) asymmetries, for instance, we find intermediate AB_2 and A_2B structures besides the pure triangular A and B lattices which are absent for hard disks. Our calculations admit more candidate phases than considered in earlier investigations [127] where two-dimensional quasicrystals were shown to be metastable. We further comment that we expect that colloidal glasses in binary mixtures of magnetic colloids [27] are metastable as well but need an enormous time to phase separate into their stable crystalline counterparts.

The model systems used in our study are binary mixtures of dipolar particles made up of two species denoted as A and B. Each component A and B is characterized by its dipole moment $\mathbf{m}_A$ and $\mathbf{m}_B$, respectively. The particles are confined to a two-dimensional plane and the dipole moments are fixed in the direction perpendicular to the plane. Thereby the dipole-dipole interaction is repulsive. Introducing the ratio $m = m_B/m_A$ of dipole strengths m_A and m_B, the pair interaction potentials between two A dipoles, a A- and B-dipole, and two B-dipoles at distance r are

$$\begin{aligned} V_{AA}(r) &= V_0\varphi(r), \quad V_{AB}(r) = V_0 m\varphi(r), \\ V_{BB}(r) &= V_0 m^2\varphi(r), \end{aligned} \tag{2.1}$$

respectively. The dimensionless function $\varphi(r)$ is equal ℓ^3/r^3, where ℓ stands for a unit length. The amplitude V_0 sets the energy scale.

Our task is to find the stable crystalline structures adopted by the system at zero temperature. We consider a parallelogram as a primitive cell which contains n_A A-particles and n_B B-particles. This cell can be described geometrically by the two lattice vectors $\mathbf{a} = a(1, 0)$ and $\mathbf{b} = a\gamma(\cos\theta, \sin\theta)$, where θ is the angle between $\mathbf{a}$ and $\mathbf{b}$ and γ is the aspect ratio ($\gamma = |\mathbf{b}|/|\mathbf{a}|$). The position of a particle i (of species A) and that of a particle j (of species B) in the parallelogram is specified by the vectors $\mathbf{r}_{\mathrm{i}}^A = (x_i^A, y_i^A)$ and $\mathbf{r}_{\mathrm{j}}^B = (x_j^B, y_j^B)$, respectively. The total internal energy (per primitive cell) U has the form

$$\begin{aligned} U = \frac{1}{2} \sum_{J=A,B} \sum_{i,j=1}^{n_J} {\sum_{\mathbf{R}}}' V_{JJ}\left(\left|\mathbf{r}_i^J - \mathbf{r}_j^J + \mathbf{R}\right|\right) \\ + \sum_{i=1}^{n_A} \sum_{j=1}^{n_B} \sum_{\mathbf{R}} V_{AB}(\left|\mathbf{r}_i^A - \mathbf{r}_j^B + \mathbf{R}\right|), \end{aligned} \tag{2.2}$$

where $\mathbf{R} = k\mathbf{a} + l\mathbf{b}$ with k and l being integers. The sums over $\mathbf{R}$ in Eq. 2.2 run over all lattice cells where the prime indicates that for $\mathbf{R} = 0$ the terms with $i = j$ are to be omitted. In order to handle efficiently the long-range nature of the dipole-dipole interaction, we employed a Lekner-summation [100, 128].

We choose to work at prescribed pressure p and zero temperature ($T = 0$). Hence, the corresponding thermodynamic potential is the Gibbs free energy G. Additionally, we consider interacting dipoles at composition $X := n_B/(n_A + n_B)$, so that the (intensive) Gibbs free energy g per particle reads: $g = g(p, m, X) = G/(n_A + n_B)$. At $T = 0$, g is related to the internal energy per particle $u = U/(n_A + n_B)$ through $g = u + p/\rho$, where the pressure p is given by $p = \rho^2(\partial u/\partial\rho)$, and $\rho = (n_A + n_B)/|\mathbf{a} \times \mathbf{b}|$ is the total particle density. The Gibbs free energy per particle g has been minimized with respect to γ, θ and the position of particles of species A and B within the primitive cell. To reduce the complexity of the energy landscape, we have limited the number of variables and considered the following candidates for our binary mixtures: A_4B, A_3B, A_2B, A_4B_2, A_3B_2, AB, A_2B_2, A_2B_3, AB_2, A_2B_4, AB_3, AB_4 and AB_6. For the AB_6 case we considered a triangular lattice formed by the A particles.

Table 2.1: The stable phases with their Bravais lattice and their basis.

Phase	Bravais lattice [basis]
$\mathbf{T}(A)$	Triangular for A [one A particle]
$\mathbf{T}(B)$	Triangular for B [one B particle]
$\mathbf{S}(AB)$	Square for A and B together [one A and one B particles]
$\mathbf{S}(A)B_n$	Square for A [one A and n B particles]
$\mathbf{Re}(A)A_mB_n$	Rectangular for A [$(m+1)$ A and n B particles]
$\mathbf{Rh}(A)A_mB_n$	Rhombic for A [$(m+1)$ A and n B particles]
$\mathbf{P}(A)AB_4$	Parallelogram for A [two A and four B particles]
$\mathbf{T}(AB_2)$	Triangular for A and B together [one A and two B particles]
$\mathbf{T}(A_2B)$	Triangular for A and B together [two A and one B particles]
$\mathbf{T}(A)B_n$	Triangular for A [one A and n B particles]

The final phase diagram in the (m, X)-plane has been obtained by using the common tangent construction. The dipole-strength ratio m can vary between zero and unity. A low value of m (i.e., close to zero) corresponds to a large dipole-strength asymmetry, whereas a high one (i.e., close to unity) indicates a weak dipole-strength asymmetry. Our calculations show that all the mixtures, except AB_3 and A_4B_2, are stable. Their corresponding crystalline lattices are depicted in figure 2.1 and the nomenclature is explained in Table 2.1. For the one component case [$X = 0$ (pure A) and $X = 1$ (pure B), see figure 2.2], we found an equilateral triangular lattice $\mathbf{T}(A)$ and $\mathbf{T}(B)$, respectively, as expected (see figure 2.1).

The most relevant and striking findings certainly concern the phase behavior at weak dipole-strength asymmetry ($0.5 \lesssim m < 1$), see figure 2.2. Thereby, the only stable mixture AB_2 over such a large range of m corresponds to the ("globally" triangular) phase $\mathbf{T}(AB_2)$ (see figure 2.1 and figure 2.2). This is in strong contrast to what occurs with hard disk potentials [15], where *no* mixture sets in at low size asymmetry. At sufficiently low dipole-strength asymmetry ($m > 0.88$), see figure 2.2, the mixture A_2B, that also corresponds to a globally triangular crystalline structure [namely $\mathbf{T}(A_2B)$, see figure 2.1], is equally stable. The stability in the limit $m \to 1$ of those globally triangular structures are fully consistent with the fact that one-component dipolar systems are triangular.

In the regime of strong dipole-strength asymmetry ($0.06 < m \lesssim 0.5$), see figure 2.2, the stability of the composition $X = 1/2$, corresponding to the mixtures AB and A_2B_2, is dominant and the phase diagram gets richer involving all the different structures [except $\mathbf{T}(AB_2)$] shown in figure 2.1. More specifically, for the composition $X = 1/2$, we have two phases $\mathbf{S}(AB)$ and $\mathbf{Rh}(A)AB_2$. The transition between these two phases is continuous as marked by a symbol # in figure 2.2. For $X = 2/3$, many stable phases emerge as depicted in figure 2.2. In the B-rich region at large asymmetry, the stability will involve many different structures which are probably not considered here. Therefore we leave this region open, see the gray box in figure 2.2. Below $X = 2/3$, at large asymmetry ($m \lesssim 0.2$), the true phase diagram will also involve a very dense spectrum of stable compositions, as suggested by the already many stable compositions (see figure 2.2), which are not among the candidate structures considered here. This feature is very similar to the behavior reported in hard disk mixtures [15], where a *continuous* spectrum of stable mixtures is found for $X \leq 2/3$ at high size asymmetry. In the limit $m \to 0$, a triangular lattice for the A particles will be stable with an increasingly complex substructure of B particles.

In conclusion, the ground-state phase diagram of a monolayer of two-dimensional dipolar particles shows a variety of different stable solid lattices. The topology of the phase diagram is different from that of hard disks. Whereas short-ranged interactions lead to a phase separation into pure A and B crystals at low asymmetries, there are two intermediate A_2B and AB_2 mixtures for softer interactions. This explains the experimental findings of Hay and coworkers [50] who found an AB_2 crystal structure in millimeter-sized steel and brass spheres [50] which does not occur to be stable for hard particles. A further more quantitative experimental confirmation of our theoretical predictions are conceivable either in suspension of magnetic colloids or for binary charged colloidal suspensions [129] confined between two parallel glass plates [21] or for any other situation where two-dimensional dipolar particles are

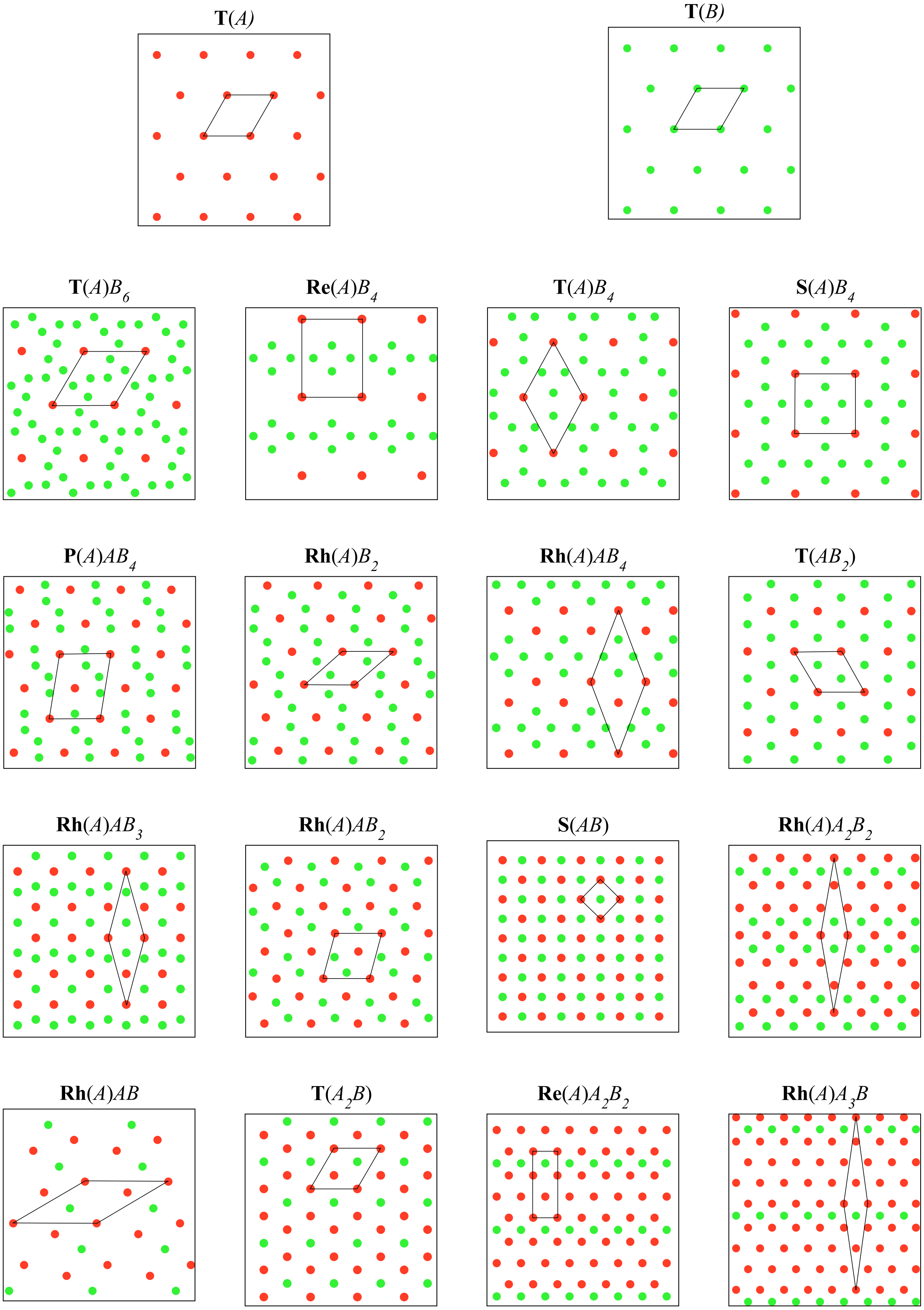

Figure 2.1: The stable binary crystal structures and their primitive cells. The red dark (green light) discs correspond to A (B) particles.

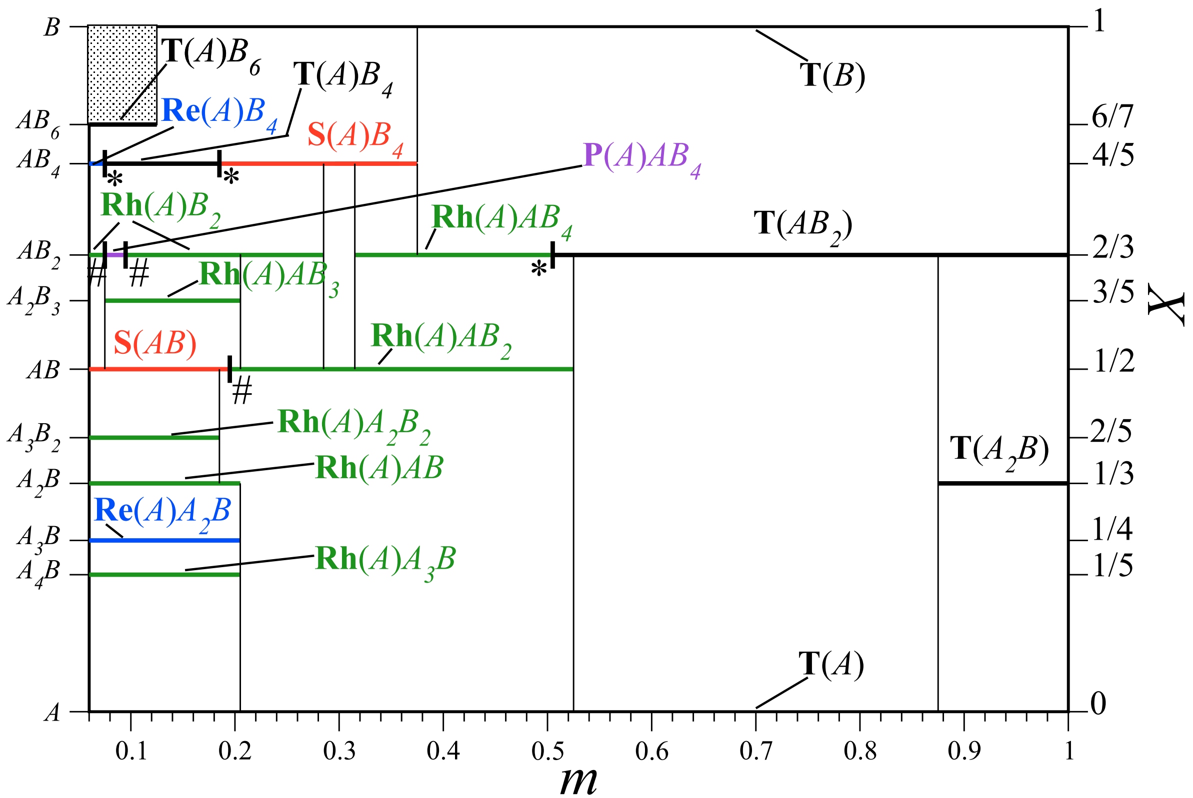

Figure 2.2: The phase diagram in the (m, X) plane of dipolar asymmetry and composition at $T = 0$. The gray box denotes an unknown region. The symbol # $(*)$ denote continuous (discontinuous) transitions.

involved.

We finish with a couple of remarks: First, based on the present studies it would be interesting to study the behavior of tilted dipoles where anisotropies and attraction play a significant role [35]. Our data may also serve as a benchmark to perform further studies on melting of the composite crystals and crystal nucleation out of the melt in two spatial dimensions. The extension to one-component bilayers [26,61] made up of dipolar particles would certainly be relevant. It would also be interesting to apply the method of evolutionary algorithms [130] to the present problem in order to increase the basket of candidate phases.

Acknowledgements

We thank Christos Likos, Hans-Joachim Schöpe and Thomas Palberg for helpful discussions. This work has been supported by the DFG within the SFB-TR6, Project Section D1.

Chapter 3

Crystal nuclei and structural correlations in two-dimensional colloidal mixtures: experiment versus simulation [1]

Abstract

We examine binary mixtures of superparamagnetic colloidal particles confined to a two-dimensional water-air interface both by real-space experiments and Monte-Carlo computer simulations at high coupling strength. In the simulations, the interaction is modelled as a pairwise dipole-dipole repulsion. While the ratio of magnetic dipole moments is fixed, the interaction strength governed by the external magnetic field and the relative composition is varied. Excellent agreement between simulation and experiment is found for the partial pair distribution functions including the fine structure of the neighbour shells at high coupling. Furthermore local crystal nuclei in the melt are identified by bond-orientational order parameters and their contribution to the pair structure is discussed.

3.1 Introduction

The mechanisms and principles of heterogeneous crystal nucleation and the subsequent microstructure formation are still far from being explored and understood [36–38]. Steering the nucleation behaviour has important implications relevant for protein crystallization [131] and the formation of new glasses and metallic alloys [132, 133]. Colloidal suspensions have been exploited as model systems for

---

[1] This chapter was published by L. Assoud, F. Ebert, P. Keim, R. Messina, G. Maret and H. Löwen in *J. Phys.: Condens. Matter 21* (2009), 464114.

crystal nucleation [134–138]. For instance, it is possible to watch crystal nucleation in real space by using confocal microscopy [139]. In particular, two-dimensional suspensions of superparamagnetic particles confined to the air-water-interface of a pending droplet [140] can easily be controlled by an external magnetic field. This allows to tune the interparticle interactions and to quench the systems quickly into a supercooled state [141]. The external field induces magnetic dipole moments in the particles [51]. If the field direction is normal to the air-water interface, the resulting dipole moments are parallel and the interparticle pair potential is repulsive scaling with the inverse cube of the particle separation [142]. Binary mixtures of these superparamagnetic colloids are ideal model systems to study crystal nucleation [30], crystallization [13] and glass formation [39] in real-space.

In this paper, we consider a binary mixture of superparamagnetic particles both by real-space microscopy experiment and Monte-Carlo computer simulations of a binary dipole-dipole interaction model [29,30]. In the simulations, the interaction is modelled as a pairwise dipole-dipole repulsion. While the ratio of magnetic dipole moments fixed, the interaction strength governed by the external magnetic field and the relative composition is varied. We compare the pair correlation functions for strong interactions (i.e. for large external magnetic fields) and find good agreement between experiment and simulations. Moreover, we discuss the occurrence of peaks in the distance-resolved pair correlations in conjunction with local crystallites. The latter are patches of triangular and square ordering which are crystalline "seeds" in the amorphous fluid and building blocks from the globally stable crystalline structure [13]. These crystallites actually could act as nucleation centers for homogeneous nucleation if the system is quenched deeply into the supercooled state [141]. Though heterogeneous nucleation is not tackled in the present paper, an understanding of the local crystallites in the bulk is a first necessary step in order to access possible pathways of inhomogeneous systems leading to heterogeneous nucleation.

As regards to previous work, we here address strong couplings different from the weakly-coupled case where partial clustering of the small particles was found [29] and equilibrated systems. In Ref. [141], a quench was performed and the pair correlation functions were found to be widely different from their equilibration counterparts. For this genuinely non-equilibrium phenomenon, Brownian dynamics computer simulations were employed.

The paper is organized as follows: in section II briefly describe the experimental set-up and the simulation method. In section III, results of experiment and computer simulations are presented and discussed. Finally we conclude in section IV.

3.2 Methods

3.2.1 Experimental system and techniques

The experimental system consists of a suspension of two kinds of spherical and superparamagnetic colloidal particles. The two species are called A and B respectively with B referring to the smaller particles. The hard-core diameters of the two species are $d_A = 4.5\,\mu m$, and $d_B = 2.8\,\mu m$ and their magnetic susceptibilities are $\chi_A = 6.2 \cdot 10^{-11}\ Am^2/T$ and $\chi_B = 6.6 \cdot 10^{-12}\ Am^2/T$. The details of the experimental set-up are explained elsewhere [30, 34, 140]. Due to their high mass density, the particles are confined by gravity to a flat water-air interface formed by a pending water drop. The droplet is suspended by surface tension in a top sealed cylindrical hole with a diameter of $6mm$ and a depth of $1mm$ of a glass plate. A coil produces a magnetic field $\mathbf{H}$ perpendicular to the water-air interface which induces a magnetic moment (i.e., $\mathbf{m}_i = \chi_i \mathbf{H}$ with $i = A, B$) in each particle. This leads to a repulsive dipole-dipole pair interaction [35]. By microscopy, trajectories of all particles in the field of view can be recorded over several days providing sufficient phase space information. The ensemble can be considered as ideally two-dimensional as the thermally activated 'out of plane' motion of the particles is in the range of a few nanometer.

While temperature is fixed to room temperature the strength of the interparticle interactions is tunable by the external magnetic field strength. A second parameter which is varied is the relative composition or the mixing ratio of the particles,

$$X \equiv \frac{N_B}{N_A + N_B} \tag{3.1}$$

3.2.2 Monte Carlo simulation technique

In our Monte Carlo computer simulations, we model the system in two spatial dimensions by a pairwise additive potential

$$u_{ij}(r) = \frac{\mu_0}{4\pi} \frac{\chi_i \chi_j H^2}{r^3} \quad (i, j = A, B), \tag{3.2}$$

where r denotes the distance between two particles. For this inverse power potential, at fixed composition X, all static quantities depend solely on a dimensionless interaction strength - or coupling constant -

$$\Gamma = \frac{\mu_0}{4\pi} \frac{\chi_A^2 H^2}{k_B T a^3} \tag{3.3}$$

where $k_B T$ is the thermal energy and $a = 1/\sqrt{\rho_A}$ the average interparticle separation between A-particles [143]. Hence effective temperature corresponds to the inverse of the coupling Γ, and the system is completely characterized by three parameters: 1) dipolar moment (or susceptibility) ratio

$$m \equiv \frac{m_B}{m_A} = \frac{\chi_B}{\chi_A}, \tag{3.4}$$

2) the relative composition X, and 3) the interaction strength Γ. While we fix the former to $m = 0.1$, the coupling Γ and the relative composition X are varied. Standard Monte-Carlo simulations were performed with $N_A = 400$ A-particles and a corresponding number N_B of B particles determined by the prescribed relative composition X. The particles are in a square box with periodic boundary conditions in both directions. Typically 4×10^6 Monte Carlo steps per particle are used for equilibration and statistics is gathered over additional 10^6 Monte Carlo steps.

3.3 Results

We present our results for the two considered compositions $X = 0.29$ and $X = 0.44$. Various coupling strengths Γ are then investigated by (i) microstructural analysis and (ii) partial pair distribution functions. In both cases, real-space experiments and Monte Carlo computer simulations have been performed. As a reference, we have gathered on table 3.1 the different stable crystalline structures at $m = 0.1$ from the ground state ($T = 0$) theoretical study [13].

3.3.1 Microstructural analysis

A visual overview of typical microstructures from the experiments are provided in figure 3.1. From the theoretical study [13] (see also table 3.1), it is known that the relevant stable ground-state crystals consist of pure A-triangular [$\mathbf{T}(A)$] structures ($X = 0$) and intersecting squares of A and B particles [$\mathbf{S}(AB)$ phase] at $X = 0.5$. Local crystallites in the fluid which possess this order are detected by coloring particles which have a pure triangular and square order[2].

---

[2] In detail, we have used criteria to define A particles which have a pure triangular surrounding of other A particles, i.e. which are close to a cut-out of a pure triangular A crystal, and, likewise, we have identified A and B particles which form locally an equimolar square lattice $S(AB)$. The corresponding two structure elements are shown in Table 3.1. In detail, we associate a triangular surrounding to an A particle if the following two criteria are fulfilled simultaneously [30]: 1) The 6-fold bond order parameter $p_6 = \sqrt{\Psi_6^* \Psi_6}$ (where $\Psi_6 = \frac{1}{6}\sum_{NN}^{6} \exp(i6\theta_{NN})$ with θ_{NN} denoting the angles of the six nearest neighbour bonds relative to a fixed reference) is larger than 0.94. 2) The relative bond length deviation $b_6 = \frac{1}{6}\sum_{NN}^{6} \frac{|l_{NN} - \bar{l}|}{\bar{l}}$ where $\bar{l}$ is the average length of the six bond lengths l_{NN} is smaller than 0.04. This double condition selects local configurations close to those of a perfect triangular lattice where p_6 is unity and b_6 vanishes. Likewise we define a square surrounding around a B particle by the criteria: 1) The 4-fold bond order parameter $p_4 = \sqrt{\Psi_4^* \Psi_4}$ (where $\Psi_4 = \frac{1}{4}\sum_{NN}^{4} \exp(i4\theta_{NN})$ with θ_{NN} denoting the bond angles of the four nearest neighbour AB bonds) is larger than 0.92. 2) The corresponding relative AB bond length deviation b_4 is smaller than 0.05.

Table 3.1: Theoretically predicted stable phases [13] for $m = 0.1$ at $T = 0$. The same notation as in Ref. [13] is used here. The disks (open circles) correspond to A (B) particles.

Phase	$\mathbf{T}(A)$	$\mathbf{R}(A)A_3B$	$\mathbf{Re}(A)A_2B$	$\mathbf{R}(A)AB$	$\mathbf{R}(A)A_2B_2$	$\mathbf{S}(AB)$
Composition (X)	0	1/5	1/4	1/3	2/5	1/2
Crystalline structures	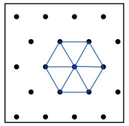	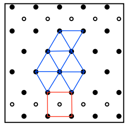	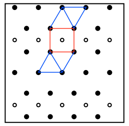	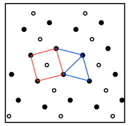	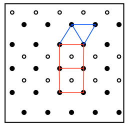	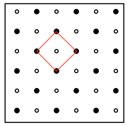

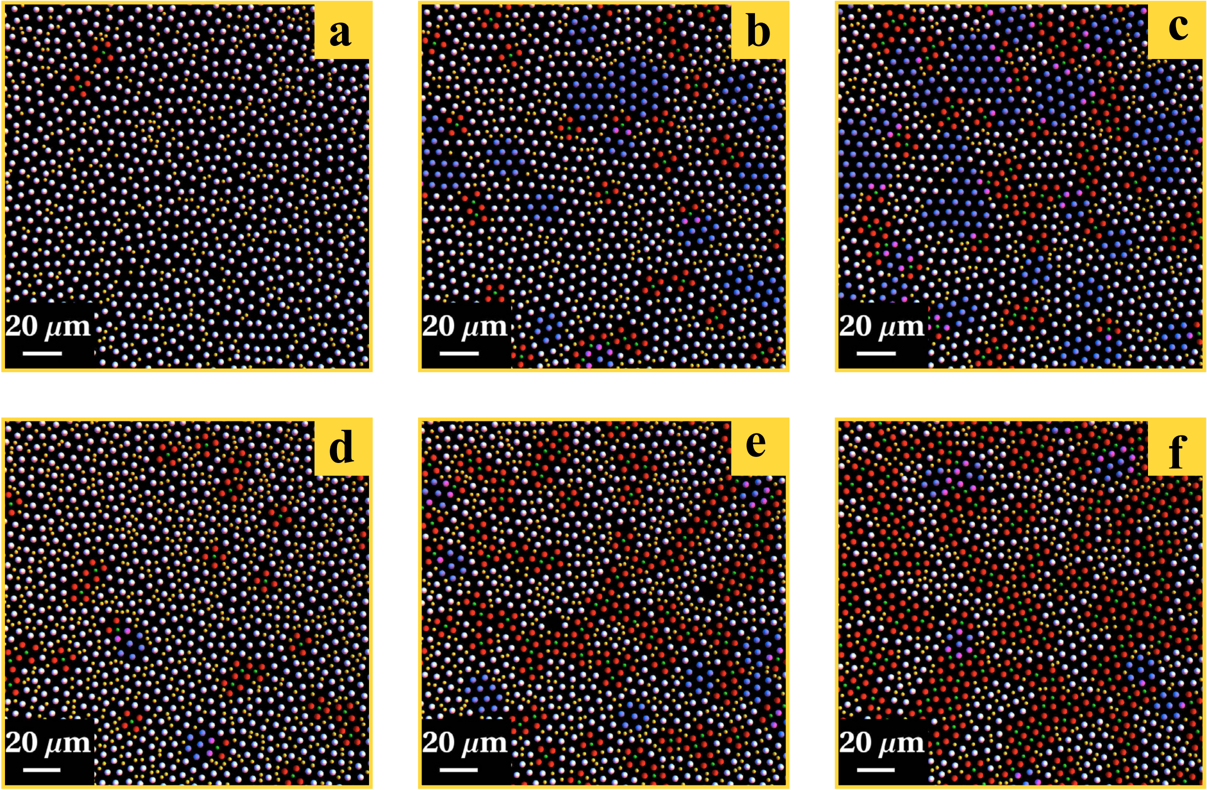

Figure 3.1: Experimental snapshots for the parameter combination (a) $X = 0.29$, $\Gamma = 4.9$ (b) $X = 0.29$, $\Gamma = 38.9$ (c) $X = 0.29$, $\Gamma = 82.9$ (d) $X = 0.44$, $\Gamma = 22.6$ (e) $X = 0.44$, $\Gamma = 49.5$ (f) $X = 0.44$, $\Gamma = 93.9$. Big particles are shown in blue if they belong to a triangular surrounding and in red if the belong to a square surrounding. All other big particles are shown in white color. Few big particles belonging to both triangular and square surroundings are shown in pink color. The small particles are shown in green if they belong to a square center of big particles, otherwise they appear in yellow.

One can clearly see from figure 3.1 that the triangular $\mathbf{T}(A)$ and square phases $\mathbf{S}(AB)$ are indeed predominant at strong enough couplings. More precisely, at $X = 0.29$, see figure 3.1 (a-c), there is a strong presence of triangular $\mathbf{T}(A)$-crystallites. This fraction of triangular crystallites is growing with increasing Γ see figure 3.1 (a-c).

At nearly equimolarity with $X = 0.44$, see figure 3.1 (d-f), the situation differs qualitatively (compare with figure 3.1 (a-c)), where we have now a strong fraction of squared $\mathbf{S}(AB)$-crystallites. This fraction is increasing with growing Γ, which is consistent with the zero temperature limit predicting the stability of the squared $\mathbf{S}(AB)$-lattice at $X = 0.5$ (see table 3.1 and Ref. [13]).

The simulation snapshots are presented in figure 3.2 for the same (Γ, X) parameters as in figure 3.1. In a general manner, there is an excellent qualitative agreement

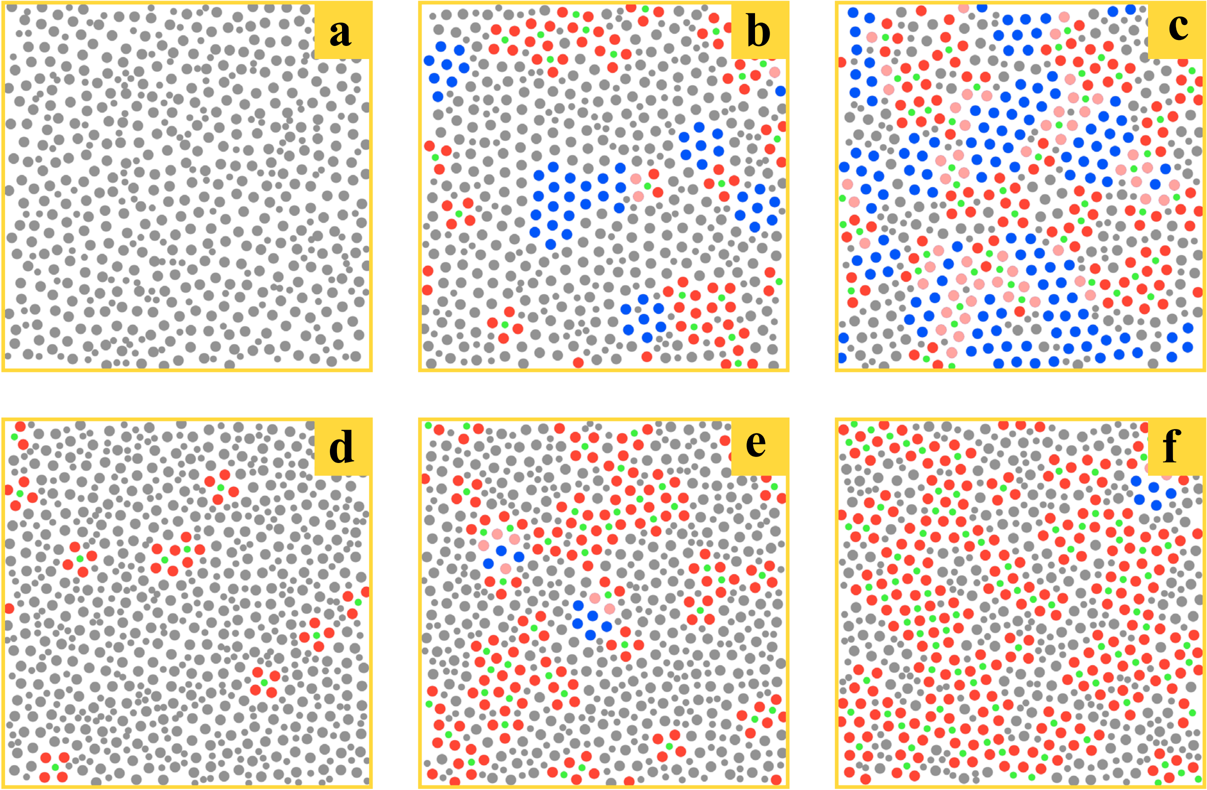

Figure 3.2: Simulation snapshots for the parameter combination (a) $X = 0.29$, $\Gamma = 4.9$ (b) $X = 0.29$, $\Gamma = 38.9$ (c) $X = 0.29$, $\Gamma = 82.9$ (d) $X = 0.44$, $\Gamma = 22.6$ (e) $X = 0.44$, $\Gamma = 49.5$ (f) $X = 0.44$, $\Gamma = 93.9$. Big particles are shown in blue if they belong to a triangular surrounding and in red if the belong to a square surrounding. All other big particles are shown in grey color. Few big particles belonging to both triangular and square surroundings are shown in pink color. The small particles are shown in green if they belong to a square center of big particles, otherwise they appear in grey.

between the experimental and simulational microstructures, compare figure 3.1 with figure 3.2. Very interestingly, the theoretically predicted intermediate rectangular phase $\mathbf{Re}(A)A_2B$, see table 3.1 for $X = 0.25$, is remarkably well present in the snapshot of figure 3.2(c). This feature was not detected in the experiments, compare with figure 3.1(c), possibly due to a slightly imperfect equilibration thereby.

The emergence of crystalline clusters in the strongly interacting system gives some insight into the nucleation behaviour. Presumably the system is in a stable crystalline phase at high Γ but since it is undercooled it does not find the ultimate stable state [144]. The intermittent crystal nucleation “self poisons” [145] further crystal growths which may be similar to nucleation in liquid crystalline systems [145].

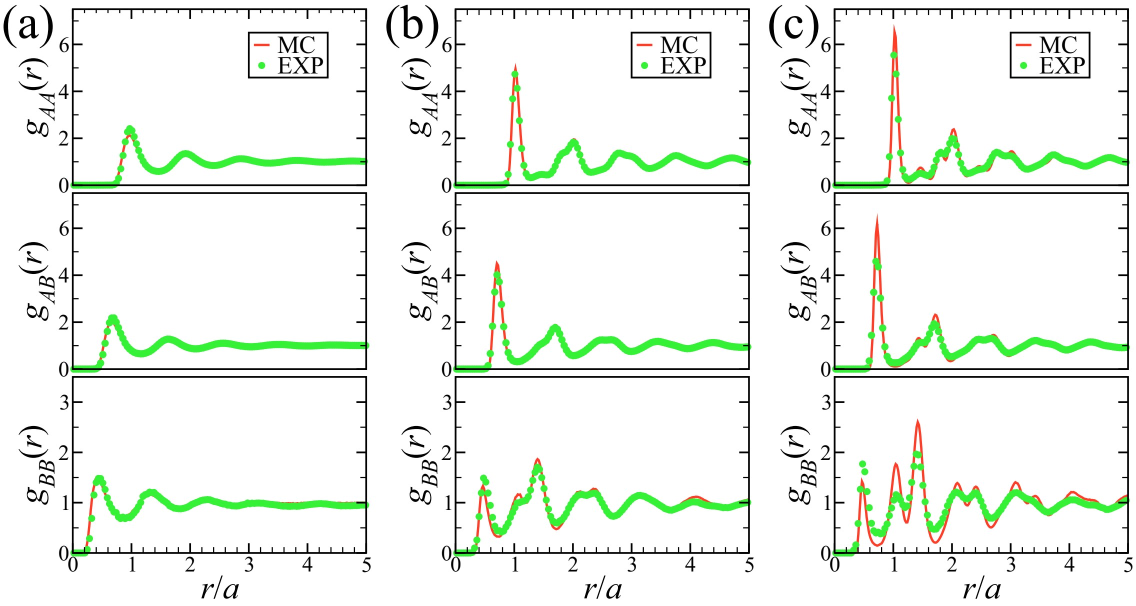

Figure 3.3: Partial radial pair-distribution functions $g_{AA}(r)$, $g_{BB}(r)$ and $g_{AB}(r)$. Experimental data (EXP) are compared to simulation results (MC) for (a) $\Gamma = 4.9$, (b) $\Gamma = 38.9$ and (c) $\Gamma = 82.9$. The composition $X = 0.29$ is fixed.

3.3.2 Pair distribution functions

We now discuss more quantitatively the structural aspects by inspecting the radially averaged partial pair distribution functions, whose corresponding microstructures can be found in figure 3.1 and figure 3.2 for the experimental and simulational data, respectively.

The case $X = 0.29$ is reported on figure 3.3. In a general fashion, there is good quantitative agreement between experiment and simulation, see figure 3.3. The only situation that slightly deviates from this quality of agreement, concerns the partial pair distribution $g_{BB}(r)$ at $\Gamma = 82.9$, see figure 3.3(c). We explain this with a small drift of the colloidal system in the field of view. The whole systems contains more than 100000 particles and is susceptible to perturbations. The drift induced some shear which may constrained here the ordering of the system at $\Gamma = 82.9$ and $X = 0.29$. The primary peaks found at $r/a = 1$ in $g_{AA}(r)$ and at $r/a = 1/\sqrt{2} \approx 0.71$ in $g_{AB}(r)$ are the signature of the squared $\mathbf{S}(AB)$-crystallites, see figure 3.3(b,c).

The disordered aspect of the material can be best identified by analyzing at the partial pair distribution $g_{BB}(r)$. Figure 3.3 (b,c) shows that the first peak in $g_{BB}(r)$ is located at $r/a \approx 0.45$, which is much smaller than the (square) unit lattice parameter, which is at $r/a = 1$. This is reminiscent to the similar trend for the small particles to form pairs and/or clusters at lower coupling [29], as can also be easily observed on the microstructures of figures 3.1 and 3.2.

The case $X = 0.44$ is reported on figure 3.4. The agreement is now even better than at $X = 0.29$, becoming perfect for all the partial distribution functions (including $g_{BB}(r)$).

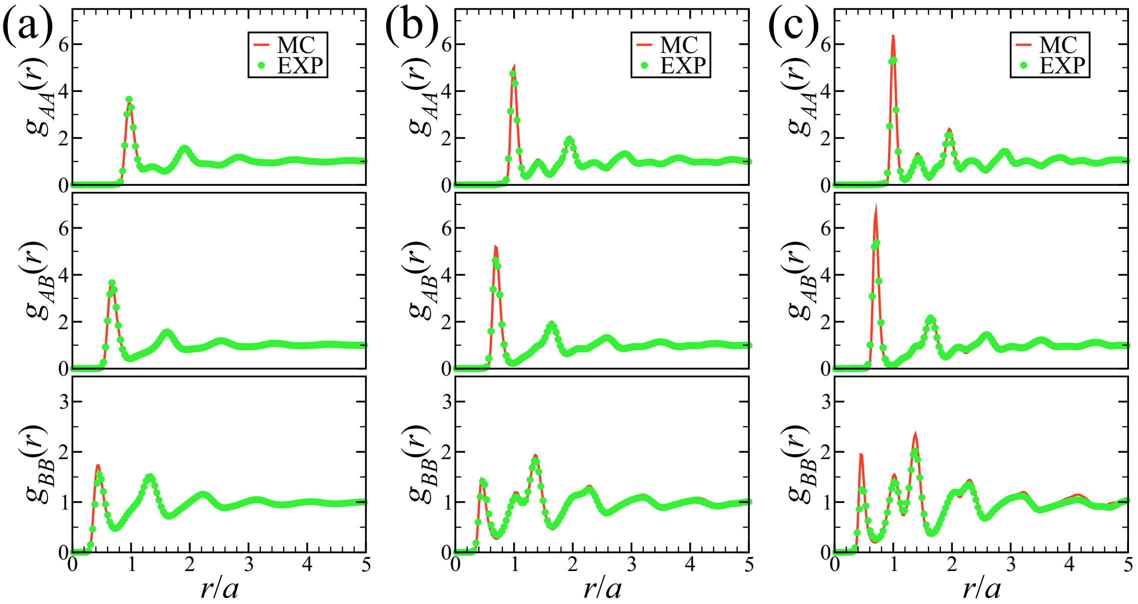

Figure 3.4: Partial radial pair-distribution functions $g_{AA}(r)$, $g_{BB}(r)$ and $g_{AB}(r)$. Experimental data (EXP) are compared to simulation results (MC) for (a) $\Gamma = 22.6$, (b) $\Gamma = 49.5$ and (c) $\Gamma = 93.9$. The composition $X = 0.44$ is fixed.

3.4 Conclusion

In conclusion we have put forward the idea that two-dimensional binary mixtures are excellent model systems for crystal nucleation as they are easily supercooled by increasing an applied external field and crystallize into a variety of crystal structures. As revealed by the excellent agreement in the pair correlation functions, the system can be modelled by a simple dipole-dipole interaction potential [35]. The strongly interacting fluid bears some crystallites which were identified and could act as possible nucleation centers both for homogeneous and heterogeneous nucleation.

Future investigations should consider the nucleation at fixed imposed nucleation seeds which was studied theoretically for one-component two-dimensional systems [146]. Steering the nucleation and growth for binary systems is expected to be much richer since there are several competing crystalline structures. Exploring more asymmetries in the magnetic moments is possible by exploiting nonlinear saturation effects in the magnetic susceptibility at high external magnetic fields. This is another parameter which is crucially determining the phase behaviour. Finally, it might be interesting to use binary charged suspensions confined between charged glass plates [77, 147] as two-dimensional model system for crystal nucleation. The interactions are then well-approximated effective Yukawa potentials [74, 148] where the screening length is steered by the salinity. Again the ground state crystal structures show a wealth of possible crystals as recently revealed by lattice-sum calculations [14]. Therefore a rich scenario of crystal nucleation and growth phenomena are expected to occur here as well. Another realization of dipolar mixtures in 2d are granular systems [149] which show interesting 2d ordering effects [150]. Finally binary colloid mixtures with added nonadsorbing polymers will result in effective attractions and possibly liquid-gas phase separation [151, 152]. The interplay of vitrification or gelation and the fluid-fluid phase separation in two-dimensions should be an interesting topic for future research [153].

Acknowledgements

We thank D.R. Nelson, Y. Terada, and P. Dillmann for helpful discussions. This work was supported by the DFG (SPP 1296, SFB-513 project B6, and SFB-TR6 project C2).

Chapter 4

Ultra-fast quenching of binary colloidal suspensions in an external magnetic field [1]

Abstract

An ultra-fast quench is applied to binary mixtures of superparamagnetic colloidal particles confined at a two-dimensional water-air interface by a sudden increase of an external magnetic field. This quench realizes a virtually instantaneous cooling which is impossible in molecular systems. Using real-space experiments, the relaxation behavior after the quench is explored. Local crystallites with triangular and square symmetry are formed on different time scales and the correlation peak amplitude of the small particles evolves nonmonotonically in time in agreement with Brownian dynamics computer simulations.

Temperature quenching belongs to the key processing techniques to produce amorphous and crystalline solids which are considerably different from their thermodynamically stable counterparts. Possible applications can be found in metallurgy, ceramics and semiconductor doping. For example, quenching is used to construct ceramic material with a high mechanical stability [154], to design resistance devices for integrated circuits [155], and to improve the optoelectronic properties of semiconductors [156].

Temperature quenching techniques are most efficient if they are performed suddenly, i.e. if the system temperature changes on a time scale that is much shorter than a time upon which a typical particle motion is performed. While this can be realized in computer simulations, see e.g. [157–159], it is practically impossible to be achieved for molecular systems where the quench is performed by a coupling to an external heat bath. There, it takes some time until the prescribed temperature

---

[1] This chapter was published by L. Assoud, F. Ebert, P. Keim, R. Messina, G. Maret, and H. Löwen in *Phys. Rev. Lett. 102* (2009), 238301.

is realized in the sample. However, as we shall show in this Letter, an ultra-fast quenching is possible for colloidal particles which move much slower and are highly susceptible to external fields.

If a suspension of superparamagnetic particles is used, an external magnetic field induces magnetic dipoles in the particles which gives rise to dipolar interactions between them [27]. In equilibrium, temperature and magnetic field strength determine the dimensionless coupling strength between the particles such that temperature is strictly equivalent to the inverse square of the magnetic field strength [29, 30]. Therefore a sudden increase of the external magnetic field corresponds to an ultra-fast quench towards lower temperature. It is important to note that the increase of the external magnetic field occurs on a time scale of a few ms much smaller than a couple of seconds typically needed by a colloidal particle to diffuse over its own size. Thereby - unlike molecular systems - colloidal systems can be exposed to ultra-fast temperature quenches.

In this Letter, we exploit this idea of quasi instantaneous quenching for a binary suspension of two-dimensional superparamagnetic colloidal particles confined to a planar water-air interface. At high temperatures - or equivalently at low external magnetic field strengths - the system is weakly correlated. After an abrupt increase of the external magnetic field, the response of the system and the early stage relaxation towards its new state is monitored by real-space imaging. For the prescribed composition of the mixture, the equilibrium state is a crystalline lattice with alternating stripes of pure triangles of the majority component and mixed squares [13]. This complicated stable crystal is not reached on the time scale explored but the system reveals structural heterogeneities corresponding to local metastable patches of crystalline order. These crystalline zones are forming on different time scales which also gives rise to nonmonotonic behaviour in time for structural correlation peaks of the small particles. The real-space experiments are in agreement with our Brownian dynamics computer simulations. Our results can be used to steer the microstructure of composite materials upon quenching and reveal the interplay between vitrification and crystal nucleation [6].

The experimental system consists of a suspension of two kinds of spherical superparamagnetic colloidal particles denoted by A and B. Those particles are characterized by different diameters ($d_A = 4.5\,\mu$m, $d_B = 2.8\,\mu$m) and magnetic susceptibilities ($\chi_A = 6.2 \times 10^{-11}$ Am^2/T, $\chi_B = 6.6 \times 10^{-12}$ Am^2/T). The relative composition $X = N_B/(N_A + N_B)$ of B particles is fixed at 40%. Due to their high mass density, the particles are confined by gravity to a flat water-air interface formed by a pending water drop. The droplet is suspended by surface tension in a top sealed cylindrical hole (6 mm diameter, 1 mm depth) on a glass plate. The system can be considered as ideally two dimensional since the thermally activated "out of plane" motion of the particles is of the order of a few tens of nanometer. A coil produces a magnetic field $\vec{H}$ perpendicular to the water-air interface inducing a magnetic moment ($\vec{m}_i = \chi_i \vec{H}$ with $i = A, B$) in each particle which leads to a repulsive dipole-dipole pair interaction of the form

$$u_{ij}(r) = \frac{\mu_0}{4\pi}\chi_i\chi_j H^2/r^3 \quad (i,j = A,B). \tag{4.1}$$

For this inverse power potential, at fixed composition X and susceptibility ratio χ_B/χ_A, all static quantities depend solely [143] on a dimensionless interaction strength (or coupling constant)

$$\Gamma = \frac{\mu_0}{4\pi}\frac{\chi_A^2 H^2}{k_B T a^3} \tag{4.2}$$

where k_BT is the thermal energy at room temperature and $a = 1/\sqrt{\rho_A}$ the average interparticle separation between A particles. The partial A particle density is set to $\rho_A = 1.97\times10^{-3}\mu\text{m}^{-2}$ so that $a \simeq 22.5\mu$m. The pair interaction is directly controlled over a wide range via the magnetic field. Making use of video microscopy, trajectories of all particles in the field of view can be recorded over several days providing the whole phase space information. The quench was realized upon suddenly rising the coupling Γ from 1 to 71 at time $t = 0$ by increasing the magnetic field. The time scale of the quench is only limited by the electronics of power supply and was measured to be 5 ms. This is much faster than the typical Brownian time $\tau = d_A^2/(4D_A)(\approx 50\text{s})$ needed for an A particle to diffuse over its own radius with $D_A = 0.11\mu\text{m}^2/\text{s}$ being the short-time diffusion constant for A particles. Hence the quench can be considered to be ultra-fast[2]. In a unquenched system clear deviations from purely diffusive behavior appear already at about $\Gamma \approx 30$ [27]. For $\Gamma = 71$ a well pronounced plateau between $t/\tau = 2$ and $t/\tau = 200$ is observed in the mean square displacement with an inflection point at $t/\tau = 40$ [27]. Additional computer simulations reveal that the equilibrium crystallization from a liquid occurs again at $\Gamma = 30$. Hence the ultra-fast quench leads deeply into the supercooled state.

In parallel, we perform nonequilibrium Brownian dynamics (BD) computer simulations[3] of our experimental system described above neglecting hydrodynamic interactions as the area fraction is small, on the 1% level. We employ point-like dipoles that interact following Eq. (4.1) with $\chi_B/\chi_A = 10\%$ and $X = 40\%$ in accordance to the experimental parameters. Knowing that the diffusion constant scales with the inverse of the radius of a particle, D_B was chosen such that $D_B/D_A = d_A/d_B$. $N_A = 400$ A particles and $N_B = 267$ B particles were placed in a square box with periodic boundary conditions applied in the two directions. A finite time step $\delta t = 6 \times 10^{-4}\tau$ was used. The early stage of the system response to the ultra-fast quench has been observed both in real-space experiments and BD computer simulations and was characterized by various time-dependent correlations. Our first aim is to identify the dynamical formation of local crystallites after the quench and detect

---

[2] For a molecular glass-former such as orthoterphenyl the time for a fast quench is about 10^9 slower than a typical molecular motion.

[3] For an equilibrium molecular dynamics simulation for a similar model, see T. Stirner, and J. Sun, Langmuir **21**, 6636 (2005).

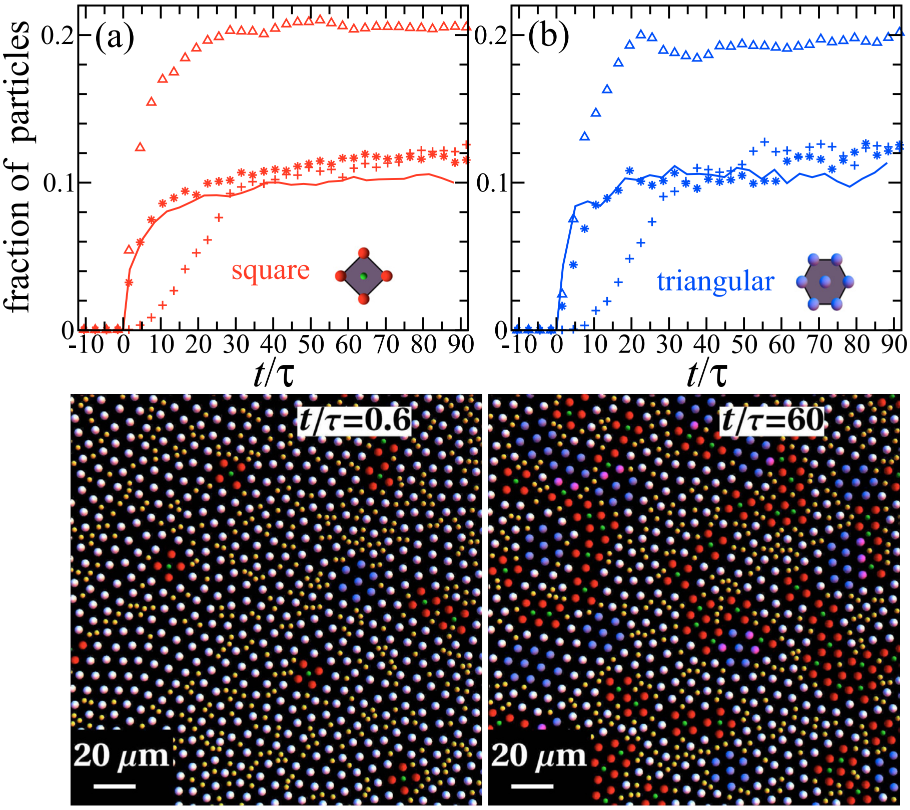

Figure 4.1: (a) Fraction of B particles belonging to a crystalline square surrounding (see inset) and (b) fraction of A particles belonging to a crystalline triangular surrounding (see inset) versus reduced time t/τ for an ultrafast quench from $\Gamma = 1$ to $\Gamma = 71$. The lines are experimental data while the symbols ($*$) are data from BD simulations. Two experimental snapshots for a time $t/\tau = 0.6$ just after the quench (left configuration) and a later time $t/\tau = 60$ (right configuration) are shown. Big particles are shown in blue if they belong to a triangular surrounding and in red if the belong to a square surrounding. All other big particles are shown in white color. Few big particles belonging to both triangular and square surroundings are shown in pink color. The small particles are shown in green if they belong to a square center of big particles, otherwise they appear in yellow. Also included are simulation data for an instantaneous "steepest descent" quench from $\Gamma = 1$ to $\Gamma = \infty$ ($\triangle$) and for a linear increase of Γ from $\Gamma = 1$ to $\Gamma = 71$ on a time scale of 30τ (+).

building blocks of the underlying equilibrium crystal. The latter consists of alternating stripes of pure A triangles and intersecting squares of A and B particles [13]. Therefore we have used criteria to define A particles which have a pure triangular surrounding of other A particles, i.e. which are close to a cut-out of a pure triangular A crystal, and, likewise, we have identified A and B particles which form locally an equimolar square lattice $S(AB)$[4]. The corresponding two structure elements are shown as insets in Figure 4.1. In detail, we associate a triangular surrounding to an A particle if the following two criteria are fulfilled simultaneously [30]: 1) The 6-fold bond order parameter $p_6 = \sqrt{\Psi_6^* \Psi_6}$ (where $\Psi_6 = \frac{1}{6}\sum_{NN}^{6} \exp(i6\theta_{NN})$ with θ_{NN} denoting the angles of the six nearest neighbour bonds relative to a fixed reference) is larger than 0.94. 2) The relative bond length deviation $b_6 = \frac{1}{6}\sum_{NN}^{6} \frac{|l_{NN}-\bar{l}|}{\bar{l}}$ where $\bar{l}$ is the average length of the six bond lengths l_{NN} is smaller than 0.04. This double condition selects local configurations close to those of a perfect triangular lattice where p_6 is unity and b_6 vanishes. Likewise we define a square surrounding around a B particle by the criteria: 1) The 4-fold bond order parameter $p_4 = \sqrt{\Psi_4^* \Psi_4}$ (where $\Psi_4 = \frac{1}{4}\sum_{NN}^{4} \exp(i4\theta_{NN})$ with θ_{NN} denoting the bond angles of the four nearest neighbour AB bonds) is larger than 0.92. 2) The corresponding relative AB bond length deviation b_4 is smaller than 0.05.

Experimental snapshots before and after the instantaneous quench are shown in Figure 4.1 with color-coded particles indicating the locations of A and B particles which belong to local triangular and square clusters. If an A particle has a triangular surrounding all seven A particles including the central one with its full surrounding are shown in blue. Conversely, if a B particle has a square surrounding it is colored in green and its four A neighbours are colored in red. All particles which belong both to the blue and red class are shown in pink. From the snapshots of Fig. 4.1, it is evident that the crystalline clusters form locally and grow as a function of time. Preferentially triangular structures form in an area depleted from B particles while square structures nucleate around "seeds" which possess a structure close to an underlying square. The resulting crystalline patches are then fluctuating with a life-time of about 30τ. The fraction of A particles with a triangular and of B particles with a square surrounding are shown as a function of time in Figure 4.1 a) and b), respectively. On the time scale considered in this plot one finds an increase from almost zero before the quench to 12 percent for the triangular A particles and the square B particles. The time scales upon which triangular and square structures are formed are different by a factor of about 2. The triangular structure is forming more rapidly than the square one. This follows from the fact that an AB square structure requires more fine-tuning of structural correlations of both species than a triangular one which can directly emerge in regions depleted from small particles. The number of pink A particles which belong to both triangular

---

[4] The selection criteria used here are more sensitive to the underlying crystal structure than the ordinary Voronoi tessellation, see J.-P. Eckmann and I. Procaccia, Phys. Rev. E **78**, 011503 (2008).

and square surroundings is growing on a time scale slightly longer than that for the square structure to a fraction of only 1-2 percent far away from the equilibrium structure where the fraction of pink particles is 2/3.

After a relaxation time of $t = 10\tau$, we have further calculated the mean-square displacements for particles which are crystalline (i.e colored in blue, red, green) and non-crystalline particles during a time of 60τ, see Figure 1. In both experiment and simulation, for both particles species the mean-square displacement of the uncolored particles is twice as large as that of the colored ones. This gives clear evidence for a correlation between local slow dynamics and local crystallinity.

By simulation we have finally explored a different depth and rate of the quench (see Fig. 1). While a "steepest descent" quench leads to a faster growth of crystalline patches and to an almost doubled crystalline fraction of particles, a linear increase of Γ within a time window of 30τ delays their formation accordingly.

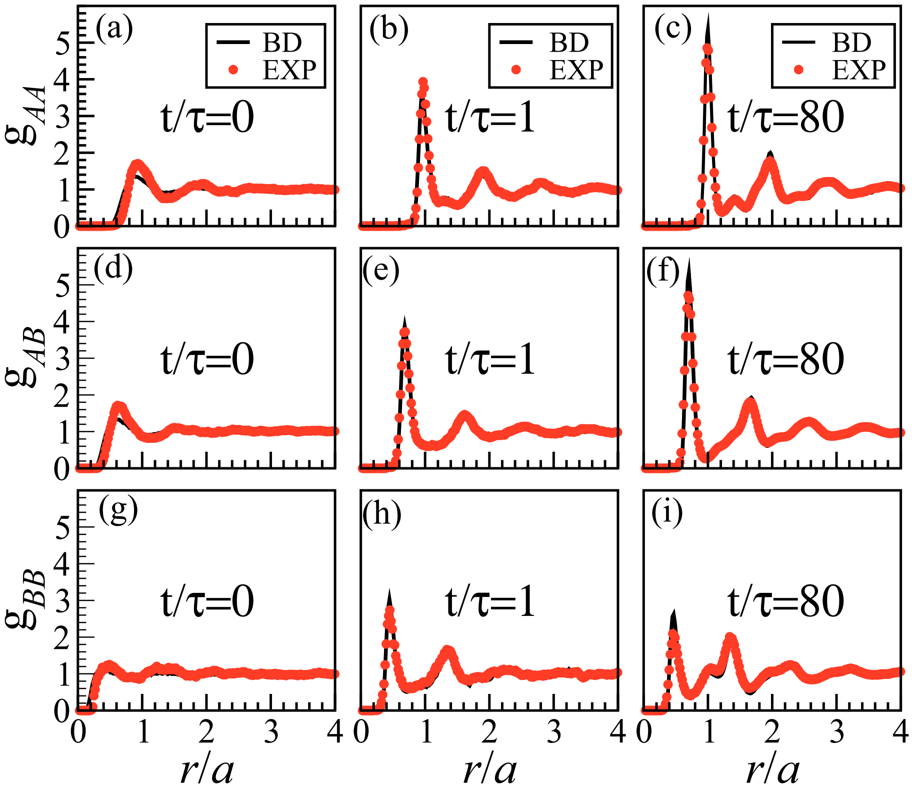

Figure 4.2: Partial pair distribution functions $g_{AA}(r)$,$g_{AB}(r)$ and $g_{BB}(r)$ of A- and B-particles versus reduced distance r/a at three different reduced times (a),(d),(g) $t/\tau = 0$; (b),(e),(h) $t/\tau = 1$; (c),(f),(i) $t/\tau = 80$. BD results (solid lines) are compared to experimental data (symbols).

Next we show the time evolution of the partial pair distribution functions $g_{AA}(r)$, $g_{AB}(r)$ and $g_{BB}(r)$ for three times $t/\tau = 0, 1, 80$ in Figure 4.2. While the correlations in the starting configurations before the quench are weak, they are quickly increasing as a function of time towards a strongly correlated glass. An averaged square order can be extracted from the growth of an intermediate peak in $g_{AA}(r)$ at $r = \sqrt{2}a$. This peak grows much slower than the first peak amplitude. The growth of the first peak amplitude in $g_{AA}(r)$ and $g_{AB}(r)$ are monotonic in time, whereas there is a non-monotonicity in that of $g_{BB}(r)$. This is clearly visible in Figure 4.3 where the dynamical evolution of the amplitudes of all three partial pair distribution function is shown. With in the statistical accuracy, the peaks of $g_{AA}(r)$ and $g_{AB}(r)$ grow on the same time scale in a monotonic way, while the peak of $g_{BB}(r)$ overshoots its final equilibrium limit, both in experiment and simulation[5]. We explain this striking effect by a two-stage relaxation process of the small particles which are first excluded from the triangular crystallites regions of the big ones. Concomitantly they show a strong correlation since they are compressed until the total system relaxes back to a state where the small particle optimize their correlations in the network dictated by the big ones.

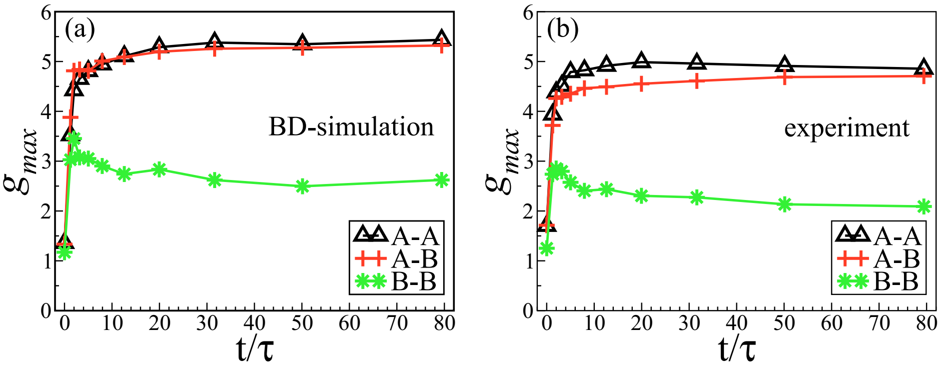

Figure 4.3: Amplitude g_{max} of the first correlation peak in the partial pair distribution function $g_{AA}(r)$ (triangles), $g_{AB}(r)$ (crosses), $g_{BB}(r)$ (stars) as a function of reduced time t/τ. Note the non-monotonicity in the amplitude of $g_{BB}(r)$. (a) Brownian dynamics data, (b) experiments.

The energetic optimization to the final state is shown in Figure 4.4. There is a huge jump in the potential energy per particle immediately after the quench which then relaxes quickly towards a transient state. Then, on a second time scale, we find a slower relaxation process accompanied by a structural ordering as can be seen in the corresponding experimental snapshots right before and after the instantaneous quench (see inset of fig. 4.4). The discrepancy between simulation and experiment for $t < 0$ may be attributed to additional interparticle forces as originating from the earth's magnetic field or other magnetic stray fields. For $t > 0$, on the other hand, there is agreement on the level of uncertainties of the particle susceptibilities.

---

[5] The overshooting disappears for slower quenching.

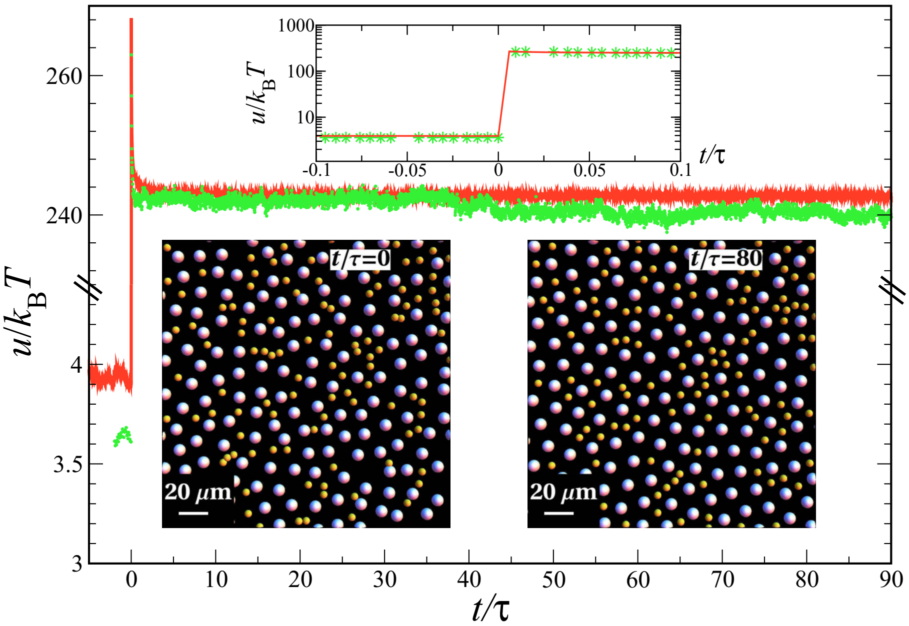

Figure 4.4: Time evolution of the potential energy u per particle in units of $k_B T$ versus reduced time t/τ. Brownian dynamics simulation data are shown in red, experimental data in green. For a better comparison the jump after the quench is truncated (see the cut in the y-axis). The inset is an expanded view. Corresponding experimental snapshots are shown before the quench at $t/\tau = 0^-$ on the left side and after the quench at $t/\tau = 80$ on the right side. Big particles are shown in white while small particles are presented as yellow spheres.

In conclusion, we have realized an ultra-fast quench in two-dimensional colloidal mixtures from a weakly interacting to a strongly interacting situation by a sudden increase of an external magnetic field which controls the interparticle repulsion. The system spontaneously relaxes by exhibiting structural inhomogeneities which reflect the underlying stable crystal and correlate with slower regions in the dynamics. The experimental data are in good agreement with Brownian dynamics computer simulations.

Our real-space characterization allows to identify the pathways of relaxation into a quenched glassy phase. As the quench is ultra-fast, the dynamical pathways are not blurred by an additional time-scale from the quench history. The built-up and the fluctuations of local crystallites after the quench can be directly followed. Therefore our analysis can help in a more fundamental way to understand the interplay between vitrification and crystallization [6]. In fact, the structural heterogeneities detected here give a considerable weight to concomitant dynamical heterogeneities [28, 160] and could therefore represent a relevant contribution to the dynamical heterogeneity of glasses [99, 161]. However, one should bear in mind that the system considered here is strongly driven and there is no aging in the glass. Finally, our results may also be useful to identify pathways of defect annealing in the crystalline phase [66, 162, 163].

Acknowledgements

Acknowledgments: We thank Patrick Dillmann for helpful discussions. This work was supported by the DFG (projects C2 and C3 of SFB TR6 and SPP 1296).

Chapter 5

Ionic mixtures in two dimensions: from regular to empty crystals [1]

Abstract

The ground state of a two-dimensional ionic mixture at zero pressure composed of oppositely charged spheres is determined as a function of the size asymmetry by using a penalty method. The cascade of stable structures includes square, triangular and rhombic crystals as well as "empty" crystals made up of dipoles and chains, which have a vanishing number density. Thereby we confirm the square structure, found experimentally on charged granulates, and predict new phases detectable in experiments on granular and colloidal matter.

Predicting the crystalline structures from first principles is one of the key problems in condensed matter physics, material science, chemistry, geophysics and polymer physics [164]. For three-dimensional ionic crystals [165, 166], it is common textbook knowledge [167] that there are three basic equimolar structures whose stability depends on the ratio of the ion radii. For increasing asymmetry in the radii, the corresponding stability sequence involves the cesium-chloride, sodium-chloride, and zincblende structures. As indicated by the names, these structures are realized in nature for the (ionic) salt crystals $CsCl$, $NaCl$ and ZnS respectively, but they show also up for a number of other equal-valency salt crystals and for mesoscopic oppositely charged colloidal particles which are suspended in a strongly deionized solvent [75, 76, 108]. The stability is rationalized by minimizing the Madelung potential energy per particle pair with respect to various periodic equimolar candidate lattices at zero temperature and zero pressure[2].

In two spatial dimensions, a similar problem arises by exploring the ground-state

---

[1] This chapter was published by L. Assoud, R. Messina, and H. Löwen in *Europhys. Lett. 80* (2010), 36001.

[2] Zero pressure is a very general case: Here the state which is formed is in coexistence with a vacuum state. Thereby, zero pressure covers a broad range of prescribed concentrations.

structure of ionic crystal monolayers in a model of oppositely charged disks with different radii. In fact, three different realizations of two-dimensional ionic crystals are possible on microscopic, mesoscopic and macroscopic length scales. First of all, crystalline sheets of molecular salts can be deposited on smooth substrates by using e.g. electrochemical methods [168]. Secondly, oppositely charged colloidal particles [75, 76] can be confined to a single layer, e.g. by using laser-optical traps [169] or suspending them at a flat fluid-fluid interface [170]. Finally, there are granulate systems of millimeter-sized metallic balls which are oppositely charged and self-organize on a macroscopic plate into crystalline arrays [171, 172]. It is important to understand the different crystalline sub-structures both from a fundamental point of view and for applications. For example, a control of the composite structures of colloidal crystals leads to new photonic [87] or phononic [173] band-gap materials, to molecular-sieves [88], to micro- and nano-filters with desired porosity [174] and to nanowires composed of individual particle strings [175]. It allows to steer protein crystallization [176].

Despite its fundamental importance, the stability of two-dimensional ionic monolayers has not been addressed for asymmetrically sized ions. Previous theoretical studies have mainly focused on ionic criticality [40] at finite temperature and on equal ion size [41]. In this Letter, we predict the ground state structures for two different relevant set-ups of oppositely charged spheres: in the first, all centers of mass belong to a common plane which corresponds to a situation where both species are confined in an interface [174]. In the second set-up, all particle surfaces touch a common plane corresponding to spheres in contact with the same planar substrate where they are confined by e.g. gravity [171, 172]. Using a novel penalty method, a wealth of different stable structures is found. These include periodic crystalline arrays, on the one hand, with square, triangular and rhombic unit cells and with both touching and non-touching large spheres. On the other hand, so-called "empty" crystals of dipoles and chains with three different internal chain structures are also stable for strong size asymmetries in the substrate set-up. In analogy to "empty liquids" [177], we refer to an "empty crystal" as a crystal with vanishing number density, or equivalently having at least one diverging lattice constant. All these structures are detectable in experiments on granular and colloidal matter and in adsorbed crystalline layers of molecular salts.

The model system used in our study are equimolar 1 : 1 mixtures of large ions (component A) with radius R_A carrying a positive charge q_A and small ions (component B) with radius R_B carrying a negative charge q_B ($|q_A| = |q_B| \equiv q$) such that the whole system is electroneutral. The size asymmetry $0 \leq R_B/R_A \leq 1$ is denoted with σ. These constitutive ions interact via a pairwise potential composed by a Coulombic and hard-core part

$$u_{\alpha\beta}(r) = \begin{cases} \frac{q_\alpha q_\beta}{r} & \text{if } r \geq R_\alpha + R_\beta \qquad (\alpha, \beta = A \text{ or } B) \\ \infty & \text{if } r < R_\alpha + R_\beta, \end{cases} \tag{5.1}$$

where r is the center-center distance between the ions α and β. The stability of the crystalline structure (at zero temperature) is ensured by steric interactions of the hardcore form. Our objective is to determine the stable structures at zero pressure and zero temperature by numerical minimization of the total potential energy.

Traditional minimization schemes [178, 179] typically require a continuous pairwise potential form in order to localize the minimum. The discontinuous hard-core potential splits the parameter space into various distinct regions which hampers straight-forward numerical minimization. For potentials which involve a hard-core part we have developed here a new technique to overcome this difficulty that relies on the so-called *penalty* method [180] which was hitherto applied to geometric packing problems of hard bodies. The key idea is to relax the non-overlap condition (i.e., $r \geq R_\alpha + R_\beta$) by introducing an auxiliary penetrable pair interaction:

$$v_{\alpha\beta}(r) = \frac{q_\alpha q_\beta}{r} + \mu \max(R_\alpha + R_\beta - r, 0), \tag{5.2}$$

where $\mu > 0$ is a penalty parameter which is larger than the gradient of the bare Coulomb potential at contact. This parameter gives a finite energy penalty to any overlapping configuration. If μ is finite but sufficiently large, the total potential energy for the auxiliary potential $v_{\alpha\beta}(r)$ has exactly the same minimal configuration as that for $u_{\alpha\beta}(r)$. However, numerically the potential energy landscape is now continuous such that standard minimization routines like the simplex algorithm [181] can be applied. Though the penalty technique itself is applicable to any spatial dimensionality and hard particle shape, we exploit it here to predict the ground state for binary hard charged spheres.

In detail, we consider a parallelogram as a primitive cell which contains n_A A-particles and n_B B-particles. We restrict ourselves to the case $n_A < 3, n_B < 3$. This cell can be described geometrically by the two spanning lattice vectors $\mathbf{a}$ and $\mathbf{b}$. The position of a particle i (of species A) and that of a particle j (of species B) in the parallelogram is specified by the vectors $\mathbf{r}_{\mathrm{i}}^A = (x_i^A, y_i^A)$ and $\mathbf{r}_{\mathrm{j}}^B = (x_j^B, y_j^B)$, respectively. Thereby, the new potential energy function that needs to be minimized at zero pressure and zero temperature as a function of the crystalline lattice parameters reads

$$\begin{aligned} U_{\text{total}} = & \frac{1}{2} \sum_{\alpha=A,B} \sum_{i,j=1}^{n_\alpha} \sum_{\mathbf{L}}{}' v_{\alpha\alpha}(\mathbf{r}_i^\alpha - \mathbf{r}_j^\alpha + \mathbf{L}) \\ & + \sum_{i=1}^{n_A} \sum_{j=1}^{n_B} \sum_{\mathbf{L}} v_{AB}(\mathbf{r}_i^A - \mathbf{r}_j^B + \mathbf{L}), \end{aligned} \tag{5.3}$$

with $\mathbf{L} = k\mathbf{a} + l\mathbf{b}$ where k and l are integers. The sums over $\mathbf{L}$ in Eqn. 5.3 run over all lattice cells where the prime indicates that for $\mathbf{L} = 0$ the terms with $i = j$ are to be omitted. In order to handle efficiently the long range nature of the Coulomb interaction, we employed a Lekner-summation [182].

We now consider two different set-ups, the "interfacial model" and the "substrate model". In the interfacial model which can be considered as a purely two-dimensional situation, the centres of all spheres are confined to a plane, see Fig. 5.1(a) for a side view of a configuration. In the substrate model, on the other hand, all spheres are touching the same underlying plane, see Fig. 5.3(a) for a side view of a configuration.

For the interfacial model, the stability phase diagram is shown versus the size asymmetry σ in Fig. 5.1(b). By increasing σ, the following phase cascade occurs:

$$\begin{gathered}\triangle(\text{touching},\ N_c=2)\rightarrow\triangle(\text{touching},\ N_c=3)\rightarrow\\ \triangle(\text{non-touching},\ N_c=3)\rightarrow Rh(\text{touching},\ N_c=3)\rightarrow\\ \square(\text{touching},\ N_c=4)\rightarrow\square(\text{non-touching},\ N_c=4)\end{gathered}$$

where the symbols $\triangle$ and $\square$ stand for triangular and square unit cells of the big ions A, respectively, and Rh corresponds to rhombic unit cells, as illustrated by the top views of the crystalline structures in Fig. 5.1(b). The topological aspect of these four phases can be discussed in terms of contact between the large spheres. More specifically, a "touching" configuration involves connected big spheres while a "non-touching" one implies disconnected big spheres, see Fig. 5.1(b). In particular, the "touching" triangular and rhombic phases are both characterized by connected A-spheres in contrast to the "non-touching" $\triangle$ and $\square$ structures which possess disconnected large spheres. Additionally, the ionic coordination number N_c defined by the number of A particles touching a single B particle, is another relevant topological characteristic.

As far as the phase transitions reported in Fig. 5.1 are concerned, the following scenario takes place. At vanishing small ion size ($\sigma\rightarrow 0$), the small ions get squeezed between two big ions so that the three centers of mass lie on a same line. The first transition $\triangle(\text{touching},\ N_c=2)\rightarrow\triangle(\text{non-touching},\ N_c=3)$ via the special structure $\triangle(\text{touching},\ N_c=3)$, characterized by an increase of the number of contacts between A and B ions, occurs at $\sigma=\frac{2}{\sqrt{3}}-1$. This special point corresponds to a compact triangular structure where a small ion has three contacts with neighbouring big ions, allowing a continuous transition[3]. The second transition, $\triangle(\text{non-touching},\ N_c=3)\rightarrow Rh(\text{touching},\ N_c=3)$, occurring at $\sigma=0.297$ is discontinuous as signaled by a jump of the angle between the two adjacent sides of the unit cell. The third transition $Rh(\text{touching},\ N_c=3)\rightarrow\square(\text{non-touching},\ N_c=4)$ via $\square(\text{touching},\ N_c=4)$, occurring at $\sigma=\sqrt{2}-1$ is continuous. A remarkable feature, en passant, is the stability of the square phase over a wide range of the size ratio σ. This structure (at $\sigma=1$) was already found in previous simulation at finite temperature and pressure in Ref [41].

For the two non-touching phases $(\triangle,\square)$ one can assign two new Madelung constants M associated to the (lattice) electrostatic energy per molecule (i.e., a pair

---

[3] A continuous transition means that the coordinates of the constitutive particles of the primitive cell change continuously.

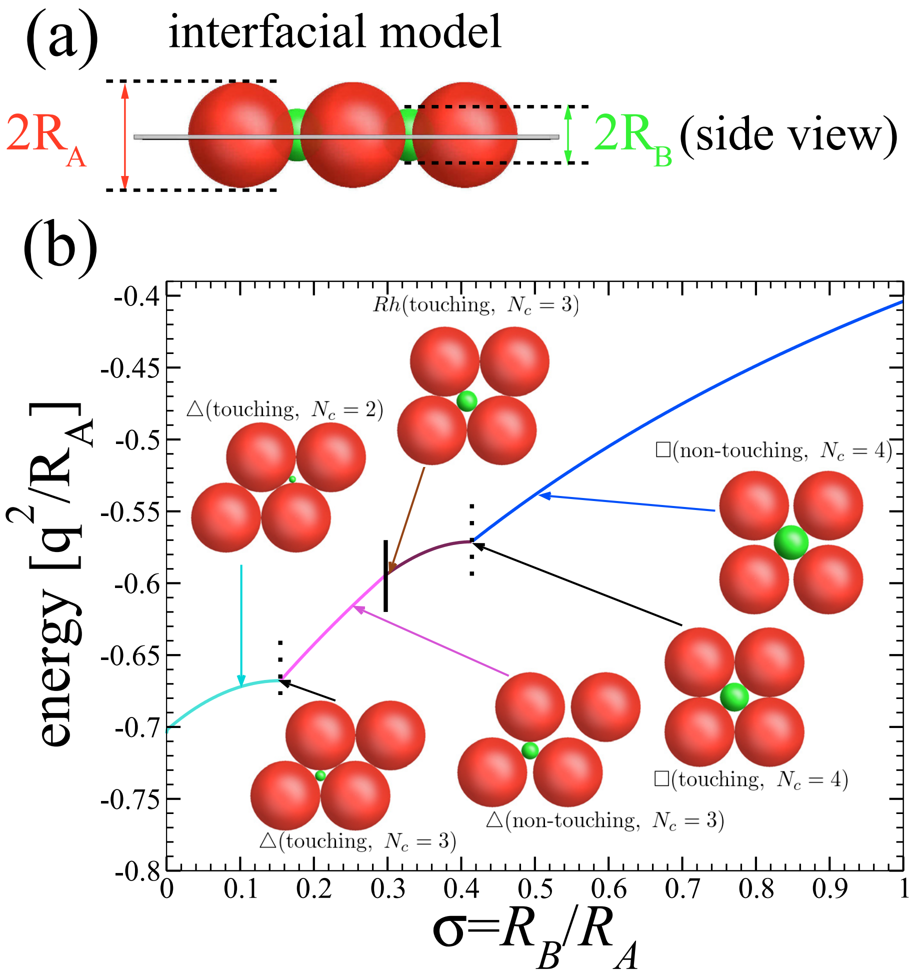

Figure 5.1: Stable structures of oppositely charged spheres versus their size asymmetry $\sigma = R_B/R_A$ in the interface model, where all sphere centers fall on the same plane: a) side-view, b) (scaled) energy per ion. The discontinuous transition is indicated by a solid bar. Continuous transitions are denoted by a broken bar. Unit cells of the corresponding stable phases are shown, where the big (small) have a radius R_A (R_B).

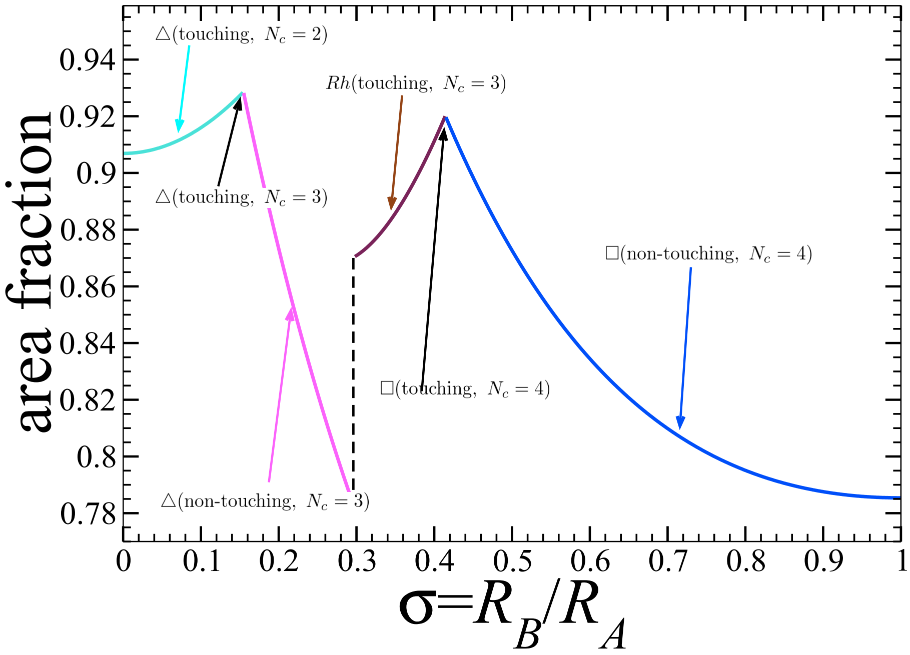

Figure 5.2: Area fraction as a function of the size aspect ratio $\sigma = R_B/R_A$.

of ions A and B) $E = -M\frac{q^2}{R_A+R_B}$. Lekner sums carried on the appropriate lattices provide:

$$M_\triangle = 1.542, \quad M_\square = 1.616$$

for the non-touching triangular and square structures, respectively. As expected, this reported value of $M_\square$ lies perfectly between that of the one dimensional lattice ($M_{1D} = 2\ln 2$) and that of a three-dimensional one ($M_{NaCl} = 1.747$).

Next we focus on the area fraction covered by the spheres which is defined as $\phi = \frac{\pi(R_A^2+R_B^2)}{S_{cell}}$, with S_{cell} being the (projected) surface of the unit cell. The results are sketched in Fig. 5.2. In the regime $\sigma < \frac{2}{\sqrt{3}} - 1$ corresponding to compact triangular structures, there is enough space to host a small ion in the interstice offered by the touching big ions, so that the profile is identical to that of pure hard disk systems, where $\phi = \frac{\pi(1+\sigma^2)}{2\sqrt{3}}$. In other words the location of the small sphere within the interstice does not alter the area fraction. For non-touching triangular structures ($\frac{2}{\sqrt{3}}-1 < \sigma < 0.297$), ϕ varies like $\frac{2\pi(1+\sigma^2)}{3\sqrt{3}(1+\sigma)^2}$. In the rhombic phase regime ($0.297 < \sigma < \sqrt{2}-1$), we have $\phi = \frac{\pi(1+\sigma^2)(1+\sigma)^2}{8\sqrt{\sigma^2+2\sigma}}$. For large enough small ions, in the square phase regime, ($\sqrt{2}-1 < \sigma < 1$), ϕ is given by $\frac{\pi(1+\sigma^2)}{2(1+\sigma)^2}$.

We finally present results for the "substrate model" where all spheres are touching the same underlying substrate plane, see Fig. 5.3(a) for a side-view. The stable crystalline structure and their energy per ion is shown in Fig. 5.3(b) versus the diameter ratio σ. For increasing size asymmetry σ, a cascade of six structures is found:

$$\begin{aligned}\text{empty crystal of dipoles (non-touching, } N_c = 1) &\rightarrow \\ \text{empty crystal of chains (non-touching, } N_c = 1) &\rightarrow \\ \text{empty crystal of chains (touching, } N_c = 1) &\rightarrow \\ \text{empty crystal of chains (touching, } N_c = 2) &\rightarrow \\ \text{empty crystal of chains (non-touching, } N_c = 2) &\rightarrow \\ \triangle(\text{non-touching, } N_c = 3) \rightarrow \square(\text{non-touching, } N_c = 4)&\end{aligned}$$

In the limit of very large asymmetry ($\sigma \rightarrow 0$), dipoles perpendicular to the substrate plane are formed. Such parallel dipoles repel each other and arrange into a crystal with diverging lattice constant and a coordination number $N_c = 1$. We call this state an "*empty crystal of dipoles*". When σ increases, the dipole moments are getting gradually tilted relative to the substrate normal until a first-order transition towards a chain composed of dipolar pairs occurs where the individual dipoles are non-touching and the coordination numbers stays at $N_c = 1$. The distance between neighbouring chains diverges since they are mutually repulsive. We are dealing therefore with an "*empty crystal of chains*" at infinite dilution, i.e. the system is periodic in the direction along the string but with a diverging interchain distance perpendicular to it bearing some analogy to smectic dipolar sheets [183]. Upon increasing σ more, the chain structure changes continuously to an internal conformation with touching large spheres (still with $N_c = 1$). This structure then transforms continuously into a chain gas of non-touching large spheres with $N_c = 2$. Then, there are two crystalline structures appearing known already from the interface model, namely a non-touching △ and a non-touching □ lattice. The former has only a tiny stability domain while the latter is stable along an enormous range of $0.517 < \sigma \leq 1$. We emphasize the striking emergence of the gas phases in the substrate model which are absent in the interface model and in three dimensions.

In conclusion, we have explored the stable ground state structures of two-dimensional ionic crystals for an "interface" and a "substrate" set-up at zero pressure. For a 1:1 oppositely charged mixture of spheres with different diameters, various stable crystalline phases were identified including regular and empty crystals of chains and dipoles. The structures of the interface set-up can be verified in suspensions of oppositely charged particles. However in charged colloidal suspensions the effective interactions are typically screened over an inverse screening length κ due to the presence of microions in the solution. For $\kappa R_A \ll 1$, the resulting phase behaviour is similar to that found here, while for strong and moderate screening the phase behaviour is not known. The substrate set-up, on the other hand, is realized for oppositely charged granular matter on a plane. Recent experiments on oppositely charged granular sheets with $\sigma \approx 1$ [171, 172] have indeed revealed a stable □(non-touching) configuration which is confirmed by our calculations. More experimental investigations on systems with higher size asymmetry are required to see

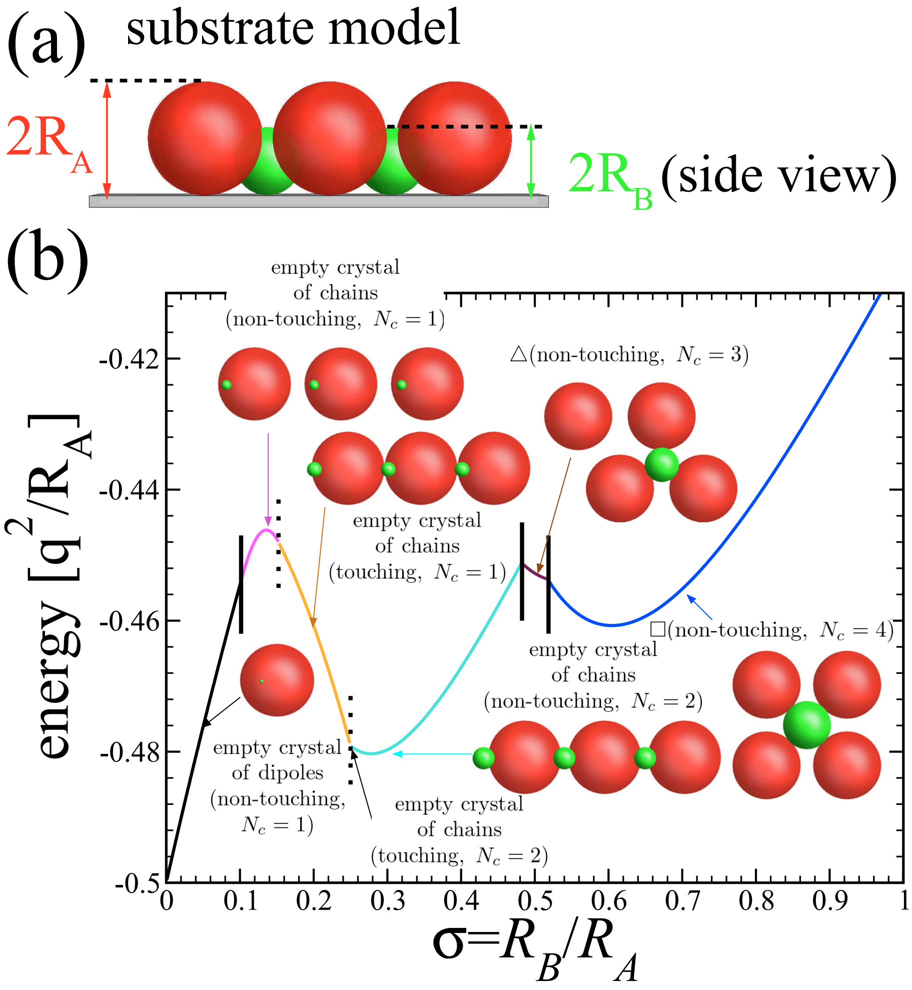

Figure 5.3: Stable structures of oppositely charged spheres versus their size asymmetry $\sigma = R_B/R_A$ in the substrate model, where all sphere surfaces touch the same plane: a) side-view, b) (scaled) energy per ion. Discontinuous transitions between the structures are indicated by a solid bar. Continuous transitions are denoted by a broken bar. Bottom views of the unit cells of the corresponding stable phases are displayed, where the big (small) have a radius R_A (R_B).

the $\triangle$(non-touching) and the predicted empty crystals of chains and dipoles. Our crystalline structures can also be verified for molecular salts. However, here a soft core description may be relevant which can alter the phase diagram.

The penalty method can in principle be applied to any other potentials which involve hard-body parts, both in two and in three dimensions. It would be interesting to see the stability phase diagram for different mixtures as e.g. colloidal hard-spheres mixtures with or without added nonadsorbing polymers.

Acknowledgements

Financial support from DFG (SFB TR6, D1) is acknowledged.

Bibliography

[1] H. Löwen, Springer Lecture Notes in Physics **74**, 139 (2006).

[2] T. Graham, Phil. Trans. Roy. Soc **151**, 183 (1861).

[3] H. Löwen, Physics Reports **237**, 249 (1994).

[4] S. M. Woodley and R. Catlow, Nature Materials **7**, 937 (2008).

[5] T. Kawasaki, T. Araki, and H. Tanaka, Phys. Rev. Lett. **99**, 215701 (2007).

[6] H. Shintani and H. Tanaka, Nature Phys. **2**, 200 (2006).

[7] A. P. Young, Phys. Rev. B **19**, 1855 (1976).

[8] D. R. Nelson and B. I. Halperin, Phys. Rev. B **19**, 2457 (1979).

[9] J. M. Kosterlitz and D. J. Thouless, J. Phys. C: Solid State Phys **6**, 1181 (1973).

[10] K. Z. R. Lenke and G. Maret, Phys. Rev. Lett **82**, 2721 (1999).

[11] K. Zahn and G. Maret, Phys. Rev. Lett **85**, 3656 (2000).

[12] C. Eisenmann *et al.*, Phys. Rev. Lett **95**, 185502 (2005).

[13] L. Assoud, R. Messina, and H. Löwen, Europhys. Lett. **80**, 48001 (2007).

[14] L. Assoud, R. Messina, and H. Löwen, J. Chem. Phys. **129**, 164511 (2008).

[15] C. N. Likos and C. L. Henley, Philos. Magas. B **68**, 85 (1993).

[16] K. Franzrahe and P. Nielaba, Phys. Rev. E **79**, 051505 (2009).

[17] E. Allahyarov, H. Löwen, and S. Trigger, Phys. Rev. E **57**, 5818 (1998).

[18] O. S. Vaulina and I. E. Dranzhevskii, Plasma Phys. Rep. **33**, 494 (2007).

[19] C. A. Murray and D. H. van Winkle, Phys. Rev. Lett. **58**, 1200 (1987).

[20] M. Brunner, C. Bechinger, W. Strepp, and V. Lobaskin, Europhys. Lett. **58**, 926 (2002).

[21] A. B. Fontecha *et al.*, J. Phys.: Condens. Matter **17**, S2779 (2005).

[22] K. Binder, J. Non-Equilib. Thermodyn. **23**, 1 (1998).

[23] C. Bechinger and E. Frey, J. Phys. Condens. Matter **13**, R321 (2001).

[24] S. Nunomura *et al.*, Phys. Rev. Lett. **89**, 035001 (2002).

[25] G. E. Morfill and A. V. Ivlev, Rev. Mod. Phys. **81**, 1353 (2009).

[26] G. Goldoni and F. M. Peeters, Phys. Rev. B **53**, 4591 (1998).

[27] H. König, R. Hund, K. Zahn, and G. Maret, Eur. Phys. J. E **18**, 287 (2005).

[28] M. Bayer *et al.*, Phys. Rev. E **76**, 011508 (2007).

[29] N. Hoffmann *et al.*, Phys. Rev. Lett. **97**, 078301 (2006).

[30] F. Ebert, P. Keim, and G. Maret, Eur. Phys. J. E **26**, 161 (2008).

[31] E. R. Weeks *et al.*, Science **287**, 627 (2000).

[32] E. R. Weeks and D. A. Weitz, Phy. Rev. Lett. **89**, 095704 (2002).

[33] V. Prasad, D. Semwogerere, and E. Weeks, J. Phys.: Cond. Mat. **19**, 113102 (2007).

[34] F. Ebert, P. Dillmann, G. Maret, and P. Keim, Rev. Sci. Instrum. **80**, 083902 (2009).

[35] V. Froltsov, R. Blaak, C. N. Likos, and H. Löwen, Phys. Rev. E **68**, 061406 (2003).

[36] A. Cacciuto, S. Auer, and D. Frenkel, Nature **428**, 400 (2004).

[37] L. Granasy, T. Pusztai, D. Saylor, and J. A. Warren, Phys. Rev. Lett. **98**, 035703 (2007).

[38] H. Emmerich, Phil. Mag. Lett. **87**, 795 (2007).

[39] H. König, R. Hund, K. Zahn, and G. Maret, Eur. Phys. J. E **18**, 287 (2005).

[40] Y. Levin and M. E. Fisher, Physica A **225**, 164 (1996).

[41] J. J. Weis, C. Levesque, and J. M. Caillol, J. Chem. Phys. **109**, 7486 (1998).

[42] G. Tammann, Ann. Phys. **40**, 237 (1913).

[43] S. Pronk and D. Frenkel, Phys. Rev. Lett. **90**, 255501 (2003).

[44] H. Xu and M. B. M, J. Phys. Condens. Matter **4**, L663 (1992).

[45] M. D. Eldridge, P. A. Madden, and D. Frenkel, Nature **365**, 35 (1993).

[46] P. Bartlett, R. H. Ottewill, and P. N. Pusey, Phys. Rev. Lett. **68**, 3801 (1992).

[47] J. Hafner, *From Hamiltonians to Phase Diagrams* (Springer, Berlin, 1987).

[48] Gompper and M. Schick, *Soft Matter, Vol. 2: Complex Colloidal Suspensions* (WILEY-VCH Verlag GmbH and Co. KGaA, Weinheim, 2006).

[49] J. Fornleitner, F. L. Verso, G. Kahl, and C. N. Likos, Soft Matter **4**, 480 (2008).

[50] M. B. Hay, R. K. Workman, and S. Manne, Phys. Rev. E **67**, 012401 (2003).

[51] K. Zahn, J. Méndez-Alcaraz, and G. Maret, Phys. Rev. Lett **79**, 175 (1997).

[52] Y. Rosenfeld, Phys. Rev. E **47**, 2676 (1993).

[53] A. A. Louis *et al.*, Phys. Rev. E **65**, 061407 (2002).

[54] E. Scholl-Paschinger and G. Kahl, J. Chem. Phys. **118**, 7414 (2003).

[55] P. Hopkins, A. J. Archer, and R. Evans, J. Chem. Phys. **124**, 054503 (2006).

[56] J. Köfinger, N. B. Wilding, and G. Kahl, J. Chem. Phys. **125**, 234503 (2006).

[57] M. A. Chavez-Rojo and M. Medina-Noyola, Physica A **366**, 55 (2006).

[58] N. Kikuchi and J. Horbach, Europhys. Lett. **77**, 26001 (2007).

[59] G. Salin and D. Gilles, J. Phys. A **39**, 4517 (2006).

[60] H. Löwen, J. Phys.: Condens. Matter **4**, 10105 (1992).

[61] R. Messina and H. Löwen, Phys. Rev. Lett. **91**, 146101 (2003).

[62] P. Hartmann, G. J. Kalman, Z. Donko, and K. Kutasi, Phys. Rev. E **72**, 026409 (2005).

[63] P. Hartmann, G. J. Kalman, and Z. Donko, J. Phys. A **39**, 4485 (2006).

[64] G. J. Kalman, P. Hartmann, Z. Donko, and M. Rosenberg, Phys. Rev. Lett. **92**, 065001 (2004).

[65] B. Liu and J. Goree, Phys. Rev. E **75**, 016405 (2007).

[66] A. Libal, C. Reichhardt, and C. J. O. Reichhardt, Phys. Rev. E **75**, 011403 (2007).

[67] K. Nelissen, B. Partoens, and F. M. Peeters, Europhys. Lett. **79**, 66001 (2007).

[68] B. Liu and J. Goree, Phys. Rev. Lett. **94**, 185002 (2005).

[69] J. M. Mendez-Alcaraz, M. Chavez-Paez, B. D'Aguanno, and R. Klein, Physica A **220**, 173 (1995).

[70] J. J. Gray and R. T. Bonnecaze, Langmuir **17**, 7935 (2001).

[71] A. Wysocki and H. Löwen, J. Phys.: Condens. Matter **16**, 7209 (2004).

[72] J. Dzubiella, G. P. Hoffmann, and H. Löwen, Phys. Rev. E **65**, 021402 (2002).

[73] E. Chang and D. Hone, Europhys. Lett. **5**, 635 (1988).

[74] E. Allahyarov, I. D'Amico, and H. Löwen, Phys. Rev. E **60**, 3199 (1999).

[75] M. E. Leunissen *et al.*, Nature **437**, 235 (2005).

[76] A. P. Hynninen *et al.*, Phys. Rev. Lett. **96**, 138308 (2006).

[77] C. A. Murray and D. G. Grier, Ann. Rev. Phys. Chem. **47**, 421 (1996).

[78] C. R. Nugent, K. V. Edmond, H. N. Patel, and E. R. Weeks, Phys. Rev. Lett. **99**, 025702 (2007).

[79] M. H. Kong, B. Partoens, and F. M. Peeters, New J. Phys. **5**, 23 (2003).

[80] G. P. Hoffmann and H. Löwen, J. Phys: Condens. Matter **12**, 7359 (2000).

[81] V. Nosenko, S. Nunomura, and J. Goree, Phys. Rev. Lett. **88**, 215002 (2002).

[82] V. Nosenko *et al.*, Phys. Rev. E **68**, 056409 (2003).

[83] H. Totsuji, T. Kishimoto, C. Totsuji, and T. Sasabe, Phys. Rev. E **58**, 7831 (1998).

[84] L. Messe *et al.*, Langmuir **18**, 4010 (2002).

[85] L. Messe *et al.*, Langmuir **18**, 9429 (2002).

[86] S. M. Clarke *et al.*, Chem. Phys. Lett. **373**, 480 (2003).

[87] V. N. Manoharan, T. Elsesser, and D. J. Pine, Science **301**, 483 (2003).

[88] J. Kecht *et al.*, Langmuir **20**, 5271 (2004).

[89] F. Yan and W. A. Goedel, Chem. Mater. **16**, 1622 (2004).

[90] A. E. Saunders and B. A. Korgel, ChemPhysChem **6**, 61 (2005).

[91] B. D'Aguanno, R. Krause, J. M. Mendez-Alcaraz, and R. Klein, J. Phys.: Condens. Matter **4**, 3077 (1992).

[92] O. S. Vaulina, O. F. Petrov, A. V. Gavrikov, and V. E. Fortov, Plasma Phys. Rep. **33**, 278 (2207).

[93] L. Bonsall and A. A. Maradudin, Phys. Rev. B **15**, 1959 (1977).

[94] H. Löwen, J. N. Roux, and J. P. Hansen, J. Phys.: Condensed Matter **3**, 997 (1991).

[95] G. E. Morfill, V. N. Tsytovich, H. Thomas, and S. V. Vladimirov, *Elementary Physics of Complex Plasmas* (Springer-Verlag GmbH, Berlin, 2008).

[96] P. N. Pusey and W. van Megen, Phys. Rev. Lett. **59**, 2083 (1987).

[97] H. N. W. Lekkerkerker *et al.*, Europhys. Lett. **20**, 559 (1992).

[98] T. Hamanaka and A. Onuki, Phys. Rev. E **74**, 011506 (2006).

[99] T. Kawasaki, T. Araki, and H. Tanaka, Phys. Rev. Lett. **99**, 215701 (2007).

[100] J. Lekner, Physica A **157**, 826 (1989).

[101] M. Mazars, Mol. Phys. **105**, 1927 (2007).

[102] J. P. Hansen, D. Levesque, and J. Zinn-Justin, *Liquids, Freezing and Glass Transition* (North-Holland, Amsterdam, 1992).

[103] B. Groh and S. Dietrich, Phys. Rev. E **63**, 021203 (2001).

[104] M. D. Eldridge, P. A. Madden, and D. Frenkel, Mol. Phys. **80**, 987 (1993).

[105] M. D. Eldridge, P. A. Madden, P. N. Pusey, and P. Bartlett, Mol. Phys. **84**, 395 (1995).

[106] M. J. Vlot, H. E. A. Huitema, A. de Vooys, and J. P. van der Eerden, J. Chem. Phys. **107**, 4345 (1997).

[107] J. R. Fernandez and P. Harrowell, Phys. Rev. E **67**, 011403 (2003).

[108] A. P. Hynninen, M. E. Leunissen, A. van Blaaderen, and M. Dijkstra, Phys. Rev. Lett. **96**, 018303 (2006).

[109] K. Zahn, J. M. MendezAlcaraz, and G. Maret, Phys. Rev. Lett. **79**, 175 (1997).

[110] K. Zahn, R. Lenke, and G. Maret, Phys. Rev. Lett. **82**, 2721 (1999).

[111] K. Zahn and G. Maret, Phys. Rev. Lett. **85**, 3656 (2000).

[112] M. Köppl *et al.*, Phys. Rev. Lett. **97**, 208302 (2007).

[113] K. Mangold, J. Birk, P. Leiderer, and C. Bechinger, Phys. Chem. Chem. Phys **6**, 1623 (2004).

[114] M. Kollmann *et al.*, Eurphys. Lett **58**, 919 (2002).

[115] N. Hoffmann, C. N. Likos, and H. Löwen, J. Phys.: Condens. Matter **18**, 10193 (2006).

[116] A. Yethiraj and A. van Blaaderen, Nature **421**, 513 (2003).

[117] R. E. Kusner, J. A. Mann, J. Kerins, and A. J. Dahm, Phys. Rev. Lett. **73**, 3113 (1994).

[118] D. P. Resendes, Phys. Rev. E **61**, 793 (2000).

[119] I. Kourakis and P. K. Shukla, Phys. Plasmas **11**, 3665 (2004).

[120] J. D. Feldmann, G. J. Kalman, and M. Rosenberg, J. Phys. A: Math. Gen. **39**, 4549 (2006).

[121] M. Seul, Europhys. Lett. **28**, 557 (1994).

[122] Y. F. Hu, K. Meleson, and J. Israelachvili, Biophysical Journal **91**, 444 (2006).

[123] S. L. Keller and H. M. McConnell, Phys. Rev. Lett. **82**, 1602 (1999).

[124] L. Messe *et al.*, Langmuir **21**, 5085 (2005).

[125] F. Elias, C. Flament, J. C. Bacri, and S. Neveu, J. Phys. I **7**, 711 (1997).

[126] H. Wiechert and B. Kromker, J. non-crystalline Solids **307**, 538 (2002).

[127] F. Scheffler, P. Maass, J. Roth, and H. Stark, Eurphys. J. B **42**, 85 (2004).

[128] A. Grzybowski and A. Brodka, Mol. Phys. **101**, 1079 (2003).

[129] P. Wette, H. J. Schöpe, and T. Palberg, J. Chem. Phys. **122**, 144901 (2005).

[130] D. Gottwald, G. Kahl, and C. N. Likos, J. Chem. Phys. **122**, 204503 (2005).

[131] E. Saridakis and N. E. Chayen, Trends in Biotechnology **27**, 99 (2009).

[132] M. C. Weinberg, G. F. Neilson, and D. R. Uhlmann, J. Non-Crystal. Solids **68**, 115 (2008).

[133] H. Emmerich, Adv. Phys. **57**, 1 (2008).

[134] H. J. Schöpe and T. Palberg, J. Phys.: Condens.Matter **14**, 11573 (2002).

[135] V. W. A. de Villeneuve *et al.*, J. Phys.: Condens.Matter **17**, S3371 (2005).

[136] S. Auer and D. Frenkel, Adv. Polym. Sci. **173**, 149 (2005).

[137] P. Wette, H. J. Schöpe, and T. Palberg, J. Chem. Phys. **123**, 174902 (2005).

[138] R. P. Sear, J. Phys.: Condens.Matter **19**, 033101 (2007).

[139] U. Gasser *et al.*, Science **292**, 258 (2001).

[140] P. Keim, G. Maret, and H. Grünberg, Phys. Rev. E **75**, 031402 (2007).

[141] L. Assoud *et al.*, Phys. Rev. Lett. **102**, 238301 (2009).

[142] For a recent work exploiting this model, see e.g.: Y. Terada, M. Tokuyama, in: AIP Conference Proceedings, **982**, 387 (2008).

[143] J.-P. Hansen and I. R. MacDonald, *Theory of Simple Liquids* (Academic, New York, 1986).

[144] F. Ebert, G. Maret, and P. Keim, Eur. Phys. J. E **29**, 311 (2009).

[145] T. Schilling and D. Frenkel, Phy. Rev. Lett. **92**, 085505 (2004).

[146] S. van Teeffelen, C. N. Likos, and H. Löwen, Phy. Rev. Lett. **100**, 108302 (2008).

[147] N. Lorenz, J. Liu, and T. Palberg, Colloid Surfaces A **319**, 109 (2008).

[148] H. Löwen and E. Allahyarov, J. Phys.: Condensed Matter **10**, 4147 (1998).

[149] M. B. Hay, R. K. Workman, and S. Manne, Phy. Rev. E **67**, 012401 (2003).

[150] D. R. Nelson, M. Rubinstein, and F. Spaepen, Philos. Mag. A **46**, 105 (1982).

[151] A. A. Louis, P. G. Bolhuis, E. J. Meijer, and J. P. Hansen, J. Chem. Phys. **117**, 1893 (2002).

[152] B. Rotenberg, J. Dzubiella, J. P. Hansen, and A. A. Louis, Mol. Phys. **102**, 1 (2004).

[153] E. Zaccarelli *et al.*, J. Phys.: Condens. Matter **20**, 494242 (2008).

[154] J. H. She, T. Ohji, and Z. Y. Deng, J. Am. Ceram. Soc. **85**, 2125 (2002).

[155] Q. Shao, G. Liu, D. Teweldebrhan, and A. A. Balandin, App. Phys. Lett. **92**, 202108 (2008).

[156] J. M. Zavada *et al.*, J. Alloys Compd. **300**, 207 (2000).

[157] R. Yamamoto and K. Nakanishi, Phys. Rev. B **49**, 14958 (1994).

[158] L. N. Yakub, Low Temp. Phys. **29**, 780 (2003).

[159] J. C. Arce, C. Schaadt, and H. J. Bart, Chem. Eng. Technol. **29**, 487 (2006).

[160] T. Hamanaka and A. Onuki, Phys. Rev. E **75**, 041503 (2007).

[161] A. Widmer-Cooper and P. Harrowell, Phys. Rev. Lett. **96**, 185701 (2006).

[162] A. Pertsinidis and X. S. Ling, Nature(London) **413**, 147 (2001).

[163] A. Pertsinidis and X. S. Ling, Phys. Rev. Lett. **87**, 098303 (2001).

[164] S. M. Woodley and R. Catlow, Nature Materials **7**, 937 (2008).

[165] E. Madelung, Phys. Z **19**, 542 (1918).

[166] P. P. Ewald, Ann. Phys. **64**, 253 (1921).

[167] See e.g.: R. C. Evans *An Introduction to Crystal Chemistry*, Cambridge University Press, pages 41-43, (1966).

[168] S. M. Rosendahl and I. J. Burgess, Electrochimica Acta **53**, 6759 (2008).

[169] M. C. Jenkins and S. U. Egelhaaf, J. Phys.: Condens. Matter **20**, 04220 (2008).

[170] C. E. McNamee *et al.*, Langmuir **21**, 10475 (2005).

[171] G. K. Kaufman *et al.*, Soft Matter **5**, 1188 (2009).

[172] G. K. Kaufman *et al.*, App. Phys. Lett. **94**, 044102 (2009).

[173] J. Baumgartl, M. Zvyagolskaya, and C. Bechinger, Phys. Rev. Lett. **99**, 205503 (2007).

[174] For uncharged particles, this was realized in: F. Yan and W. A. Goedel, Chem. Mater. **16**,1622 (2004); Nano Lett. **4**,1193 (2004).

[175] G. W. Cho K. S., Talapin D. V. and M. C. B., J. Am. Chem. Soc. **127**, 7140 (2005).

[176] E. S. Nagayama K., Takeda S. and Y. H., Jpn. J. Appl. **34**, 3947 (1995).

[177] E. Bianchi *et al.*, Phys. Rev. Lett. **97**, 168301 (2006).

[178] D. Gottwald, C. N. Likos, G. Kahl, and L. H., Phys. Rev. Lett. **92**, 068301 (2004).

[179] L. Filion and M. Dijkstra, Phys. Rev. E **79**, 046714 (2009).

[180] A. V. Fiacco and G. P. McCormick, *Nonlinear Programming: Sequential Unconstrained Minimization Technique* (John Wiley and Sons, New York, 1968).

[181] J. A. Nelder and R. Mead, Computer Journal **7**, 308 (1965).

[182] A. Grzybowski and A. Brodka, Mol. Phys. **100**, 1017 (2002).

[183] C. Eisenmann, U. Gasser, P. Keim, and M. G., Phys. Rev. Lett. **93**, 105702 (2004).